

Intrinsic AGN SED & black hole growth in the Palomar–Green quasars

Caterina Lani¹★, Hagai Netzer¹ and Dieter Lutz²

¹*School of Physics and Astronomy, Tel Aviv University, Tel Aviv 69978, Israel*

²*Max-Planck-Institut für extraterrestrische Physik, Giessenbachstraße, 85748 Garching, Germany*

Accepted 2017 June 1. Received 2017 May 28; in original form 2017 February 26

ABSTRACT

We present a new analysis of the PG quasar sample based on *Spitzer* and *Herschel* observations. (I) Assuming PAH-based star formation luminosities (L_{SF}) similar to [Symeonidis et al. \(2016, S16\)](#), we find mean and median intrinsic AGN spectral energy distributions (SEDs). These, in the FIR, appear hotter and significantly less luminous than the S16 mean intrinsic AGN SED. The differences are mostly due to our normalization of the individual SEDs, that properly accounts for a small number of very FIR-luminous quasars. Our median, PAH-based SED represents $\sim 6\%$ increase on the $1 - 243\mu\text{m}$ luminosity of the extended [Mor & Netzer \(2012, EM12\)](#) torus SED, while S16 find a significantly larger difference. It requires large-scale dust with $T \sim 20 - 30\text{ K}$ which, if optically thin and heated by the AGN, would be outside the host galaxy. (II) We also explore the black hole and stellar mass growths, using L_{SF} estimates from fitting *Herschel*/PACS observations after subtracting the EM12 torus contribution. We use rough estimates of stellar mass, based on scaling relations, to divide our sample into groups: on, below and above the star formation main sequence (SFMS). Objects on the SFMS show a strong correlation between star formation luminosity and AGN bolometric luminosity, with a logarithmic slope of ~ 0.7 . Finally we derive the relative duty cycles of this and another sample of very luminous AGN at $z = 2 - 3.5$. Large differences in this quantity indicate different evolutionary pathways for these two populations characterised by significantly different black hole masses.

Key words: galaxies: active – quasars: supermassive black holes – galaxies: star formation

1 INTRODUCTION

A long-standing quest in the field of extra-galactic astronomy is the understanding of how Active Galactic Nuclei (AGNs) and their host galaxies impact on the respective evolution.

The well-known correlation between the mass of the central Super Massive Black Hole (SMBH) and the velocity dispersion of the bulge of its host ($M - \sigma$ relation; [Ferrarese & Merritt 2000](#), [Gebhardt et al. 2000](#)) led to the postulation of a scenario where feedback, driven by the central SMBH, impacts on the galactic environment and ultimately regulates the bulge’s star formation activity and mass growth. Although the exact relationship is still highly debated (e.g. [Kormendy & Ho 2013](#), [Läsker et al. 2014a](#), [Läsker et al. 2014b](#), [Reines & Volonteri 2015](#), [Läsker et al. 2016](#), [Shankar et al. 2016](#)), this is an indication that the evo-

lution of the host galaxy and that of the central SMBH may be closely related.

Both star formation activity and black hole (BH) accretion feed from the same materials. Although these processes take place on very different spatial (typically sub-parsec for the BH accretion and kpc for star formation activity) and temporal (typically a few million years for the BH accretion and a few hundreds million years for star formation activity) scales, they may compete for their fuel. In favour of an evolution “in tandem” for these two processes, is the observation that the cosmic star formation rate density, and the cosmic accretion activity of SMBHs, rise and fall at a similar pace, with both peaking at around redshift $z \sim 2$ (e.g. [Madau et al. 1996](#); [Ueda et al. 2003](#); [Heckman et al. 2004](#); [Hopkins & Beacom 2006](#); [Madau & Dickinson 2014](#)). We caution, however, that this picture only holds when the overall galaxy population is considered. In contrast, when only the most luminous quasars in the Universe are taken into consideration, star formation activity and BH accretion

★ E-mail: caterina@wise.tau.ac.il

appear to peak at different redshift ($z \sim 4$ for the former and $z \sim 2.5$ for the latter, e.g. [Netzer et al. 2016](#)). This may be an indication that BHs with significantly different masses evolve along different pathways with respect to their hosts.

One avenue to observationally explore a potential co-evolution is to consider the black hole accretion rate and star formation activity in AGNs and their hosts, over a range in redshift and AGN bolometric luminosity. This is a difficult task because it requires the determination of the relative contribution from star formation and black hole accretion to the NIR–MIR BH+host SED. A variety of methods has been used to tackle this issue. Some consider polycyclic aromatic hydrocarbons (PAHs) spectral features ($\lambda = 6\text{--}13\ \mu\text{m}$), as these originate in the proximity of young massive stars and therefore constitute good tracers of pure star formation activity (e.g. [Gillett et al. 1975](#); [Willner et al. 1977](#); [Genzel et al. 1998](#); [Laurent et al. 2000](#); [Sturm et al. 2000](#); [Hernán-Caballero et al. 2015](#); [García-Bernete et al. 2015](#)). Given that the conversion from PAH flux to SF is non-trivial, and given that the use of PAH features requires spectroscopic data, many studies prefer SED fitting as a mean to estimate the star formation activity in AGN hosts. This approach requires far infrared (FIR) and millimeter observations. It also necessitates prior-knowledge (or assumption) of both the shape and contribution of the intrinsic AGN emission to the overall AGN+host SED.

As explained, the PAH-based method relies on MIR spectroscopy to identify the most appropriate SF template (from a wide range of libraries) which, in turn, is used to subtract the flux attributable to SF in the host galaxy from the AGN+host SED. The result is therefore the intrinsic AGN SED. Unsurprisingly, this procedure does not yield an uncertainty-free intrinsic AGN SED. For example, accurate estimates for the equivalent width of the $7.7\ \mu\text{m}$ PAH feature is difficult due to its blending with the neighbouring $8.6\ \mu\text{m}$ feature. Most works converge on a typical intrinsic AGN SED shape, characterised by two broad bumps at ~ 10 and $\sim 20\text{--}40\ \mu\text{m}$ due to silicate emission, and a fast decay long-ward of the second silicate feature. The slope of the decay and the exact location of the turn-off can however strongly vary from one work to the next. Some find the turn-off is located at about $\lambda > 30\ \mu\text{m}$ (e.g. [Netzer et al. 2007](#); [Mor & Netzer 2012](#); [Xu et al. 2015](#); [Lyu & Rieke 2017](#)), others find it at moderately longer wavelengths depending on AGN luminosity (e.g. [Mullaney et al. 2011](#)) and at much longer wavelengths (e.g. [Symeonidis et al. 2016](#) at $\sim 100\ \mu\text{m}$). The intrinsic uncertainty and difficulties involved in the accurate determination of star-formation with PAHs in AGNs are the most likely culprits for the observed discrepancies. In order to test the turn-off and slope of the intrinsic AGN SED in the FIR, [Netzer et al. \(2016\)](#) considered a large number of FIR upper limits for the most luminous quasars at redshift $z = 2 - 3.5$ ($\log L_{\text{AGN}} \geq 46.5$), and found that these are fully consistent with the extended [Mor & Netzer \(2012\)](#) intrinsic AGN SED (see §3 and [Netzer et al. 2016](#)), mostly consistent with the [Mullaney et al. \(2011\)](#) intrinsic AGN SED (that based on the more luminous sources in their sample, $\log(L_{2\text{--}10\text{KeV}}) \geq 42.9$) and inconsistent with the [Polletta et al. \(2006, 2007\)](#) SED as used by [Tsai et al. \(2015\)](#).

Very recently [Lyu et al. \(2017\)](#) considered the entire sample of Palomar–Green quasars ([Schmidt & Green 1983](#))

and identified a secure sub-sample (~ 10 per cent) of sources that show evidence of warm/hot dust deficiency in their NIR–MIR SEDs. Regardless of their spectral shape at shorter wavelengths these quasars show a FIR decay that is broadly consistent with earlier works (e.g. [Xu et al. 2015](#); [Netzer et al. 2016](#)), but starts at shorter wavelengths ($2 - 5\ \mu\text{m}$) and is steeper. We note that these IR-weak sources had already been identified, although not as systematically characterised, in [Mor & Trakhtenbrot \(2011\)](#) and [Mor & Netzer \(2012\)](#). Despite the consideration of nearly an identical sample in the current work and in [Lyu et al. \(2017\)](#), we focus on the longer wavelengths (FIR) of the intrinsic AGN SED. We will, therefore, not discuss the results from [Lyu et al. \(2017\)](#) on this specific topic any further in the remainder of this work.

Irrespective of the differences in the adopted intrinsic AGN SEDs, the sample selection methods and the treatment of the data in hand (e.g. survival analysis vs. stacking), a plethora of works has identified some general trends of AGN luminosity ($\equiv L_{\text{AGN}}$ hereafter) with SF luminosity (obtained by integrating the relevant SF templates between $8\ \mu\text{m}$ and $1000\ \mu\text{m}$, L_{SF} hereafter). On the one hand, in the regime where AGN activity dominates, i.e. $L_{\text{AGN}} > L_{\text{SF}}$, there are hints for a correlation: $L_{\text{SF}} \propto L_{\text{AGN}}^{0.6\text{--}0.7}$ (e.g. [Netzer 2009](#); [Rosario et al. 2012](#); [Netzer et al. 2016](#); [Ichikawa et al. 2016](#)), at least in the local Universe. Some studies confirm the persistence of this correlation at high redshift (e.g. $z = 2 - 3.5$, [Mullaney et al. 2012](#); [Rovilos et al. 2012](#); [Netzer et al. 2016](#)), while others point towards its disappearance for $z > 1$ (e.g. [Rosario et al. 2012](#); [Stanley et al. 2015](#)). On the other hand, there is on average a close to linear relation, $L_{\text{SF}} \sim L_{\text{AGN}}$, for FIR selected samples (e.g. [Mullaney et al. 2012](#); [Chen et al. 2013](#); [Delvecchio et al. 2015](#)), and no significant correlation for X-ray selected samples (e.g. [Rosario et al. 2012](#); [Stanley et al. 2015](#); [Shimizu et al. 2016](#)).

The same matter can be analysed in terms of the ratio between star formation rate (SFR) and black hole accretion rate (BHAR), e.g. [Mullaney et al. \(2012\)](#). This represents the instantaneous growth of stellar mass to that of the black hole. For example [Netzer et al. \(2016\)](#) found that the most luminous AGNs in the redshift range $z \sim 2 - 3.5$, that are detected in *Herschel*/SPIRE, show a ratio of SFR/BHAR similar to the ratio of stellar mass to black hole mass observed in the local Universe for the most massive, spheroidal galaxies. This is consistent with a scenario where the most luminous sources in the Universe have built up a significant fraction of their stellar mass during periods when the black hole was extremely active.

In this paper we focus on the well-studied sample of Palomar–Green quasars ([Schmidt & Green 1983](#)) and their recent *Herschel*¹ observations. This allows us to extend the study by [Netzer et al. \(2016\)](#) to a sample of black holes with lower mass and at lower redshift, with the aim of determining how their behaviour differs from that of the most massive

¹ *Herschel* is an ESA space observatory with science instruments provided by European-led Principal Investigator consortia and with important participation from NASA.

BHs. Furthermore, we make use of their extensive spectroscopic and photometric data to revisit the intrinsic AGN SED shape.²

The sample, the data and basic quantities (i.e. BH mass) are described in §2. The two sets of SF luminosities (PAH-based and SED-fitting-based) considered in our work, a new median PAH-based intrinsic AGN SED, and our SED fitting decomposition method are detailed in §3. In §4 we discuss our findings. In §4.1 we contrast the two sets of SF luminosities dealt with in this work, while in §4.2 we characterise the new median PAH-based intrinsic AGN SED. In §4.3 we investigate the typical covering factor that we found for the PG sample, and in §4.4 that of the potential non-torus-related, non-SF-related dust. We conclude by focusing on the relative instantaneous growth rates of BH and stellar mass in §4.5, where we also consider results from a previous study in order to gain a more complete understanding of these quantities over a range in redshift and AGN luminosity/BH mass. Our results are summarised in §5. Throughout this paper we assume $H_0 = 70 \text{ km s}^{-1} \text{ Mpc}^{-1}$, $\Omega_M = 0.3$ and $\Omega_\Lambda = 0.7$.

2 SAMPLE AND DATA

2.1 Sample

We consider a sample of Palomar–Green Quasars (PG QSOs), which was in turn selected from the Palomar Bright Quasar Survey Catalogue from Schmidt & Green (1983). While below we summarise its characteristic, we refer the reader to Schmidt & Green (1983), Petric et al. (2015) and references therein for more details regarding this sample.

PG QSOs are optically luminous (B -band magnitude $M_B < 16.16$), blue type-I quasars. Their optical colour is $U - B < -0.44$ (Schmidt & Green 1983), their redshifts range from $z \sim 0$ to $z \sim 0.5$ (Boroson & Green 1992), and their black hole masses and Eddington ratios cover the ranges $M_{\text{BH}} = 4 \times 10^6 - 2 \times 10^9 M_\odot$ and $L_{\text{AGN}}/L_{\text{Edd}} = 0.01 - 1.2$ respectively (for details on how we measured these quantities see §2.2). All these properties are illustrated in Figure 1. While the L_{5100} values employed in our work were not corrected for host galaxy contamination, the observed $EW(H\beta)$ distribution suggests a typical host galaxy contamination to L_{5100} of ~ 20 per cent. Finally, Jester et al. (2005) show that, although incomplete in $U - B$, PG QSOs are representative of the general population of optically-bright, optically-selected quasars.

2.2 Data

In our work we make use of both photometric and spectroscopic IR data. The former cover the following wavelength range: NIR from the 2MASS survey (Skrutskie et al. 2006); MIR from *WISE* (Wright et al. 2010) and FIR from the

Herschel Space Observatory (Pilbratt et al. 2010). In particular, the J , H , K and *WISE* data were taken from the NASA/IPAC IR science archive, from the 2MASS All-Sky Point Source Catalog and the AllWISE Source Catalog respectively. Far-infrared 70, 100, and $160\mu\text{m}$ *Herschel*/PACS (Poglitsch et al. 2010) data were retrieved from the *Herschel* archive and reduced as described in and used for Lutz et al. (2016). In summary, we used a standard “masked high-pass filtering” reduction with a circular mask centered on the source position. Fluxes are measured by aperture photometry, and noise is estimated by placing additional apertures in regions off the source. Most sources were observed twice to obtain both 70 and $100\mu\text{m}$ photometry, and the parallel $160\mu\text{m}$ results for these were averaged. In two cases we do not quote a $160\mu\text{m}$ flux due to blending with a nearby source. Furthermore, no PACS observations are in the *Herschel* archive for PG1226+023 and PG1444+407. Most observations of PG QSOs have been obtained in program OT1_lho_1 (see Petric et al. 2015 for first results), with a few others from OT1_hnetzer_1 and OT1_rmshotz_1 (see Meléndez et al. 2014). The 250, 350, and $500\mu\text{m}$ *Herschel*/SPIRE data were taken from (Petric et al. 2015, their Table 1).

The spectroscopic data were taken from Shi et al. (2014) and are a compilation of spectra observed as part of a programme (PID: 5096, PI: Rieke), and archive spectra. The data reduction and processing are described in detail in Shi et al. (2014). Here we only provide the reader with a summary. All spectra but one (see later) are the combination of the short-low ($5 - 14 \mu\text{m}$; SL) and long-low ($14 - 40 \mu\text{m}$; LL) resolution observations by *Spitzer*/IRS. For a given source, the SL spectrum was aligned to the LL spectrum and, in turn, the result was aligned to the *Spitzer* $24 \mu\text{m}$ photometric point. This procedure was necessary due to slight calibration differences; Shi et al. (2014) report that the scaling factors are close to unity in the majority of cases (their Table 2). We confirm that the Shi et al. (2014) spectra are in good agreement with the *Spitzer* $24 \mu\text{m}$ photometric points that we have downloaded from the NASA/IPAC Infrared Science Archive.

In order to extract the photometric information required for our SED fitting procedure, we consider the following three wavelength bands: $6.75 - 7.25 \mu\text{m}$, $20.75 - 21.25 \mu\text{m}$ and $29.75 - 30.25 \mu\text{m}$ (all rest-frame). These were chosen to be approximately equally spaced across the spectrum, as well as avoid strong emission and absorption lines. Our SED fitting procedure uses the median fluxes in these regions. We have not considered the *Herschel*/SPIRE data (provided by Petric et al. 2015) in our SED fitting procedure (§3.1) as they are mostly upper limits, especially in the higher redshift ($z > 0.2$) sources. When possible, however, we consider the *Herschel*/SPIRE $250 \mu\text{m}$ information in our PAH-based calculation of the median intrinsic AGN SED (§3.3). The PAH-based SF luminosities considered in §3.2 and 3.3 are taken from Shi et al. (2007). They were preferred to those presented in Shi et al. (2014) which are based on a combination of information from the $11.3\mu\text{m}$ PAH feature (solely due to SF) and FIR photometry (including emission from both SF and AGN-heated dust), therefore potentially introducing another source of uncertainty in our analysis. We note that adopting the Shi et al. (2014) results would lead to larger SF luminosities and lower FIR AGN continua than derived

² A new paper by Lyu & Rieke (2017) appeared on the arXiv two days before we received our referee report. The paper addresses several issues we also discuss in this work and a complete reference to all these would completely alter the structure of our manuscript. Because of this, we only refer to the main points that are relevant to the present work, mostly at the end of §4.

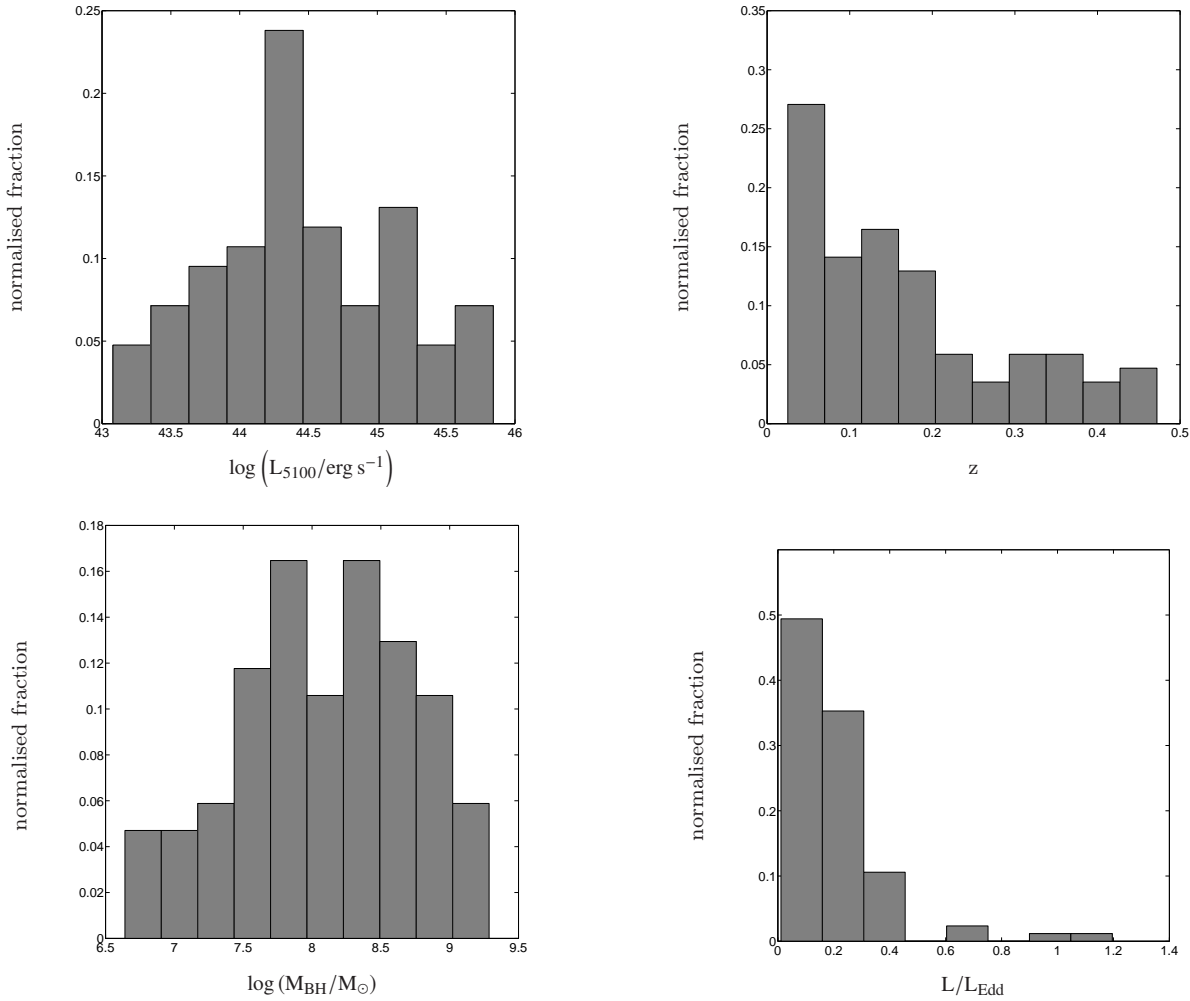


Figure 1. The four histograms show the properties of the PG quasars sample considered in the current work. The top left panel shows the normalised fraction of objects as a function of optical (at 5100) luminosity (not corrected for host galaxy contamination, see §2.1), while the top right panel shows that as a function of redshift. The bottom panels show the normalised fraction of PG quasars as a function of black hole mass (left) and Eddington ratio (right). The description of how the quantities along the x-axes were measured is provided in §2.2.

with the [Shi et al. \(2007\)](#) results. Lower intrinsic AGN continua would also be a consequence of adopting a PAH to SF scaling such as that in [Lyu & Rieke \(2017\)](#) instead of that from [Shi et al. \(2007\)](#). All BH masses used in this work are based on the most recent reverberation mapping results of [Bentz et al. \(2013\)](#) and the FWHM of the $H\beta$ line. We considered the following equation:

$$M_{\text{BH}} = 1.4625 \times 10^5 f_{\text{BLR}} \left(\frac{\text{FWHM}(H\beta)}{10^3 \text{ km/s}} \right)^2 R_{\text{BLR}}, \quad (1)$$

where $\text{FWHM}(H\beta)$ is the full width half maximum intensity of $H\beta$. R_{BLR} is the size of the broad line region and can be approximated by $K \left(\frac{L_{5100}}{10^{44}} \right)^\alpha$; following [Bentz et al. \(2013\)](#) we set K and α to 33.65 and 0.53 respectively. Finally, f_{BLR} , which contains information about the geometry and dynamics of the broad line region gas, was set to 1.

Regarding the bolometric luminosity L_{AGN} , we used the expression from [Netzer \(2013\)](#) which gives the following bolometric correction factor, bol , that multiplies L_{5100} : $\text{bol} = 53 - \log(L_{5100})$. This is in very good agreement with other estimates for objects in the general luminosity range of the PG sample but tends to over-estimate L_{AGN} for more luminous sources (see discussion in [Netzer et al. 2016](#)).

Our final sample consists of 85 PG QSOs; of these 69 were detected in all the three *Herschel*/PACS bands (though 2 suffer from blending at $160\mu\text{m}$), 12 are undetected in one and/or two of the *Herschel*/PACS bands, 4 are undetected in all *Herschel*/PACS bands. The original PG QSOs sample ([Schmidt & Green 1983](#)) contained 87 quasars, but [Petric et al. \(2015\)](#) only obtained *Herschel* data for 85 of them. We note that PG0003–199 lacks the LL *Spitzer*/IRS observation and we find a large discrepancy between its spec-

trum and the full SED. For this source we therefore chose not to consider the information from *Spitzer*/IRS.

3 MEASURING SF LUMINOSITIES AND INTRINSIC AGN SEDS

The goals of this work are: (i) accurately measuring SF luminosities for all PG quasars, (ii) defining the intrinsic AGN SED of these sources, and (iii) investigating the growth rate of the stellar mass and BH mass in the sample. Our SF luminosity measurements are based on two independent methods. The first rests on the assumption that the intrinsic AGN SED of all sources is well-described by the extended version of the empirical median template identified by [Mor & Netzer \(2012\)](#). This, together with the relevant 25th and 75th percentiles, was obtained by considering a sample of ~ 100 local AGNs. The [Mor & Netzer \(2012\)](#) approach was based on a combination of PAH spectroscopy from *Spitzer*, with NIR and FIR photometry of different origin (see their paper for more details). They subtracted, from the overall spectrum, one of 40 FIR SF templates, ensuring that the only flux left around the $7.7\ \mu\text{m}$ aromatic feature was consistent with the noise level. This resulted in three SEDs covering the rest frame wavelength $\lambda_{\text{rest}} = 1 - 30\ \mu\text{m}$: a median SED and two others representing the 25th and 75th percentiles from it. In later works (e.g. [Netzer et al. 2014, 2016](#)), this was extended to longer wavelengths based on various clumpy torus models. The procedure involved adding a 100 K modified blackbody, with $\beta = 1.5$, to the [Mor & Netzer \(2012\)](#) templates. Hereafter we will refer to this template as the extended [Mor & Netzer \(2012, EM12\)](#) SED. Although [Mor & Netzer \(2012\)](#) considered PAH features in their analysis, they took a different approach from [Shi et al. \(2007, see §3.2\)](#), requiring no assumption for the conversion from PAH to SF luminosity. The resulting median intrinsic AGN SED and the corresponding 25th and 75th percentiles are showed in [Figure 2](#) (black and grey lines). It is important to note that these SEDs are meant to represent the combination of dust emission from the central torus and that from the narrow line region (NLR). Because of the modified blackbody extrapolation beyond $30\ \mu\text{m}$, they do not consider the possibility of AGN heated dust at a distance far beyond that of the NLR, and hence a temperature below 100 K. In the reminder of this manuscript, when we mention “torus” (e.g. torus luminosity, torus covering factor) in the context of the EM12 SED we actually mean “torus+NLR”.

There is mounting observational evidence in favour of the EM12 intrinsic AGN SED, especially if one assumes a narrow range in SED shape (a “universal” SED). [Netzer et al. \(2016\)](#) used a sample of 66 *Herschel*/SPIRE-non-detections to provide constraints on the intrinsic FIR AGN SED. They found the EM12 intrinsic AGN SED to be consistent with the information provided by all the non-detections in their sample. They also showed that given a universal SED, the [Mullaney et al. \(2011\)](#) set of templates is consistent with a significant number of *Herschel* upper limits, and the [Polletta et al. \(2006, 2007\)](#) SED, as used by [Tsai et al. \(2015\)](#), is inconsistent with the majority of the observations. We note, however, that the samples considered by [Mor & Netzer \(2012\)](#), [Netzer et al. \(2016\)](#) and the current work, are significantly more luminous than the

sources in [Mullaney et al. \(2011\)](#), thus making a direct comparison of their results problematic. In addition, and as already pointed out in the literature (e.g. [Lyu & Rieke 2017](#)), unlike the current work and the others mentioned above, [Polletta et al. \(2006, 2007\)](#) do not explicitly correct for the star formation contribution in the FIR, making the comparison irrelevant. For these reasons, when in the remainder of this manuscript we examine the central issue of intrinsic AGN SED, we will mostly contrast the EM12 SED with that determined on a sub-sample of the sources considered here ([Symeonidis et al. 2016](#)). Finally the only direct, high resolution sub-mm observations of the nuclear obscuring structure to date (in NGC 1068, e.g. [García-Burillo et al. 2016; Gallimore et al. 2016](#)) are consistent with the EM12 intrinsic AGN SED. This remains the case even allowing for small differences due to aperture size and the fact that NGC 1068 is a type-II AGN.

[Figure 2](#) shows the location of the $20\ \mu\text{m}$ -normalised luminosities calculated from the data in hand for our parent sample of PG QSOs, with respect to two intrinsic AGN SEDs. In solid black we show the EM12 SED and in green the mean SED suggested by [Symeonidis et al. \(2016, hereafter S16\)](#). There is good agreement between the data and both intrinsic AGN templates in the near- and mid- IR. If we focus on the longer wavelengths, i.e. *Herschel*/PACS and *Herschel*/SPIRE, the situation looks different. We find (see [Appendix](#)) that the different shape of the S16 SED at this wavelengths is mostly due to the way it was calculated. In their work S16 start by calculating the *mean* observed quasar SED without normalising the individual SEDs at a given wavelength. This returns a mean observed quasar SED which is heavily weighted towards the more luminous sources (their PG sample spans nearly two orders of magnitude in luminosity). They later obtain the *mean* SF template for this ensemble, made from all the individual SF templates, and subtract it from the mean observed spectrum to derive the *mean* intrinsic AGN SED. From [Figure 2](#) it is apparent that, even prior to subtracting the appropriate emission due to SF from the *Herschel*/PACS data, the suggestion that the S16 AGN SED is universal is inconsistent with the observations because ~ 50 per cent of our PG QSOs already lie below this. The EM12 median intrinsic AGN SED seems a better representation of the general AGN population if, indeed, emission heated by the AGN is dominated by warm dust in the torus and NLR, and can be considered universal. In [§4.2](#), we attempt to repeat the S16 procedure, with several important modifications, and discuss the meaning of the mean intrinsic AGN SED obtained by them.

The first set of SF luminosities we consider in this work was obtained by adopting the EM12 median SED and the two accompanying SEDs representing the 25th and 75th percentiles, as our best representation of the intrinsic AGN SED ([§3.1](#)). The second, independent set of SF luminosities was that estimated by [Shi et al. \(2007\)](#). This method does not assume a particular intrinsic AGN SED, but a relation between the luminosity of PAH features as measured from the *Spitzer* spectroscopy, and the total infrared ($8 - 1000\ \mu\text{m}$) luminosity. This method is the only one used by S16 in their recent analysis of the PG sample. We note that in their paper S16 focus on those PG quasars at redshift $z < 0.18$ in order to cap the number of upper limits in their analysis. In the current work, however, we focus on the full sample, but

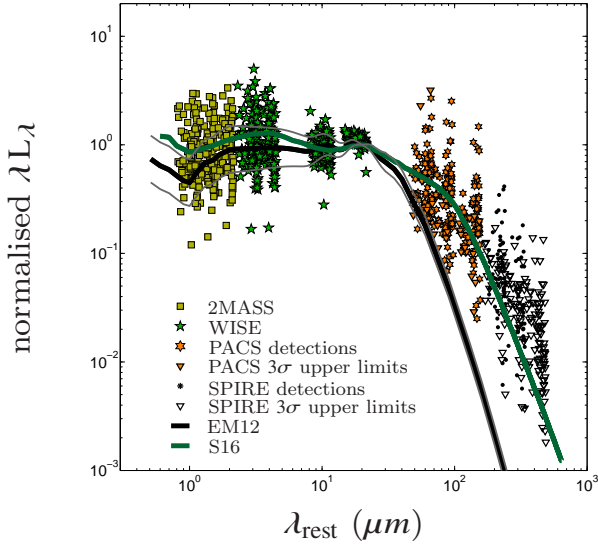


Figure 2. Two different intrinsic AGN SEDs: in green is that found by S16, and in black the extended version of the Mor & Netzer (2012, EM12) SED with corresponding 25th and 75th percentiles (light grey). Over-plotted are the normalised luminosities for our sample which include both AGN and host emission.

present the analysis of the same sample as that consider by S16 in the Appendix.

3.1 Measuring SF luminosities assuming the EM12 intrinsic AGN SED

Here we estimate the SF activity for 81 PG QSOs (those with at least one 3σ -*Herschel*/PACS detection) by assuming the extended Mor & Netzer (2012) intrinsic AGN SED discussed above, and employing a SED fitting method.

First we estimate the torus luminosity by fitting the three intrinsic AGN SED models (median and 25th and 75th percentiles) to the near- and mid-infrared points ($2.15 \mu\text{m} \leq \lambda_{\text{rest}} \leq 30 \mu\text{m}$) of the object’s SED. Given the redshift range of our sources, this includes the data from WISE and the photometric points extracted from the *Spitzer*/IRS spectra. This window in wavelength-space is where the intrinsic AGN emission dominates over that from the host. We do not consider the emission short-ward of $\lambda_{\text{rest}} = 2 \mu\text{m}$ as this is where the contamination from the host’s old stellar population can be significant; furthermore, the accretion disk emission at longer wavelengths is negligible (see e.g. Hernán-Caballero et al. 2015). We avoid combining the MIR and FIR into a single χ^2 fit, and instead use a least square procedure for the MIR for two reasons. First, the formal uncertainties on the *Spitzer* and *WISE* points are much smaller than the scatter in the MIR data. Second, the uncertainties on the *Herschel* FIR data are much larger and combining the two into a single χ^2 procedure will heavily bias the results.

Upon determining the best fitting EM12 SED, we know its contribution to the total SED at wavelengths $\lambda_{\text{rest}} \geq 30 \mu\text{m}$. This quantity is then subtracted from the composite AGN+host SED in the wavelength range covered by *Her-*

schel/PACS ($70 \mu\text{m} \leq \lambda_{\text{obs}} \leq 160 \mu\text{m}$), such that the remaining luminosity can be associated with star formation alone. The star-formation luminosity (L_{SF}) is estimated using the Chary & Elbaz (2001, CE01 hereafter) templates for local star-forming galaxies. There is evidence (e.g. Elbaz et al. 2010) for the CE01 templates underestimating the SF emission at wavelength $\lambda_{\text{rest}} > 150 \mu\text{m}$. We note, however, that for all our sources 2 ($70 \mu\text{m}$ and $100 \mu\text{m}$) out of the 3 PACS points considered in the SED fitting are at wavelength $\lambda_{\text{rest}} < 150 \mu\text{m}$, and for ~ 70 per cent of our sources the last PACS point ($160 \mu\text{m}$) is short-ward of $\lambda_{\text{rest}} = 150 \mu\text{m}$. Furthermore, the errorbars accompanying the $160 \mu\text{m}$ point are typically larger than those at shorter wavelengths. The effect of underestimating the SF emission at long wavelengths by the CE01 templates, albeit present, is therefore within this uncertainty. As a test investigating the impact that the consideration of the alternative Dale & Helou (2002) set of SF templates has on the main conclusions of our work we refer the reader to §3.3. In our routine we fit both for the vertical normalisation (i.e. L_{SF}) and the template shape (dust temperature). This is achieved by normalising each CE01 template by its total ($\lambda = 8 - 1000 \mu\text{m}$) IR luminosity prior to considering them in the fitting procedure. In this part of the fitting we minimise the χ^2 , searching for the best fitting combination of L_{SF} and template. Our fitting is comprised of two phases. First we look for the CE01 SF template nearest to the torus-subtracted FIR luminosity, and then we search the CE01 library within ± 0.5 dex of the SF luminosity of such template to improve the match in shape. The uncertainty in L_{SF} is determined by marginalising over the best fitting CE01 template shape, and identifying the lowest and highest L_{SF} among those that satisfy the equation $\chi^2 < \chi_{\text{min}}^2 + 1$. For further details on our method, as well as on the treatment of uncertainties, we refer the reader to Netzer et al. (2016).

In Figure 3 we show two examples of SED fits, one where there is significant star formation (left panel) and one where the majority of the FIR emission can be attribute to torus+NLR emission (right panel). We note that 4 sources (PG1022+519, PG1244+026, PG1351+236, and PG2304+042) have unsuccessful fits, due to peculiar NIR–MIR SED shapes. These were excluded from the remainder of our work.

3.2 Estimating star formation luminosities using PAH features

As previously mentioned, this method relies on the existence of a widely-used relation between PAH luminosity and SF luminosity (e.g. Roussel et al. 2001; Förster Schreiber et al. 2004; Wu et al. 2005), which remains uncertain due to the large intrinsic scatter and dependence on SF luminosity and metallicity (e.g. Calzetti et al. 2007; Smith et al. 2007). Shi et al. (2007) measured PAH luminosities for the PG quasars and then determined the L_{SF} values later considered by S16 in their work, and that we consider here.

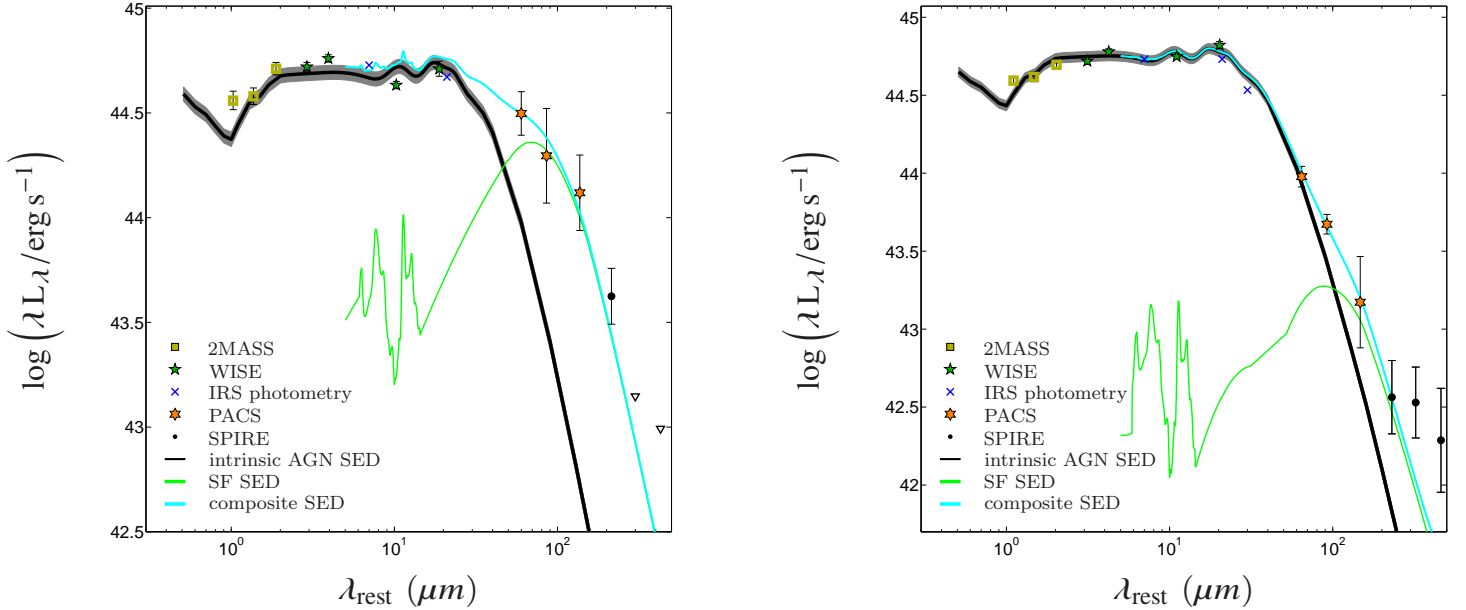


Figure 3. Examples of SED fits; PG1322+659 (left panel) and PG1211+143 (right panel). The point-like symbols refer to the same instruments as those in Figure 2, and the downward pointing triangles represent 3σ upper limits. The black line corresponds to the best fitting EM12 template, and the grey shaded area corresponds to its uncertainty (see §3.1). The green line represents the best fitting SF template from the CE01 set. The PG QSO in the left panel shows significant SF, while that in the right panel does not and most of its FIR emission is consistent with dusty torus+NLR emission.

Figure 4 compares the star formation luminosities obtained from the two methods (SED fitting and aromatic features). For clarity we omit the PGs that, based on the work by Shi et al. (2007), are upper limits in PAH-based SF luminosities. We find a median difference of 0.34 dex between the two sets of SF luminosities. As shown in the next section, this has important implications on the estimated intrinsic AGN SED shape.

3.3 The PAH-based intrinsic AGN SED

The dataset considered here is superior to that considered in Mor & Netzer (2012). First, all objects have high quality *Spitzer*/IRS spectra. Second, all objects have *Herschel*/PACS data, and third the sample is much better defined and hence represents better the population of luminous, local AGNs. As explained, though, the EM12 SED has been derived by arbitrarily adding a single temperature ($T = 100$ K) modified blackbody to the already-known SED at short wavelength. As we show below, this is found to be consistent with the SED of many sources. The method, however, is limited in its ability to investigate the *range* of intrinsic SEDs characterizing the entire population. For this reason one needs an independent way to estimate SF luminosities. Despite its limitations, the PAH-based method indeed constitutes such a tool, hence we use it here keeping in mind the large associated uncertainties.

In this part of the analysis we consider the PAH-based SF luminosities provided by Shi et al. (2007) when these are

not upper limits. If the Shi et al. (2007) estimates are upper limits we consider the L_{SF} values from our SED fitting as long as they are not larger. We followed this approach as we believe our L_{SF} to be the most reliable/accurate estimates available in these cases. For those 11 upper limits where our estimated SF luminosities are larger than those provided by Shi et al. (2007) we follow the same procedure as S16, thus subtracting the SF templates corresponding to 1/2 of the Shi et al. (2007) upper limit.

Our analysis of the PAH-based intrinsic AGN SED consists of a simple subtraction of a SF template from the overall SED, on an object by object basis. Specifically, for a given value of L_{SF} , we find the template with the closest SF luminosity $L_{\text{SF,nearest}}$ in the CE01 library. We then scale the chosen template by the ratio $L_{\text{SF}}/L_{\text{SF,nearest}}$. The result is then subtracted from the overall, observed AGN SED which has been previously interpolated between $5\mu\text{m}$ and the longest wavelength where we have a flux detection.

There are four main differences between the current work and that of S16. First, we use *Herschel*/PACS photometry in all three bands, while S16 used the less reliable *Spitzer* and *AKARI* photometry in the wavelength range $\lambda = 70\text{--}100\mu\text{m}$ (and *Herschel*/PACS at $\lambda = 160\mu\text{m}$). A direct comparison between their *Spitzer* $70\mu\text{m}$ and our *Herschel* $70\mu\text{m}$ photometries shows that the latter is higher for ~ 60 percent of the sources. In addition, several sources that are upper limits in the *Spitzer* bands, are detections in the corresponding *Herschel* bands. We emphasize that *Herschel* provides much improved photometric accuracy, and better sampling of the $40\text{--}250\mu\text{m}$ range, compared to *Spitzer* and

Table 1. Quantities for our PG QSOs sample.

<i>Name</i>	<i>RA</i> (deg)	<i>Dec</i> (deg)	<i>z</i>	$\log L_{5100}^{(a)}$ (ergs^{-1})	$\log M_{\text{BH}}$ (M_{\odot})	$\log L_{5\mu\text{m}}$ (ergs^{-1})	$\log L_{\text{SF}}$ (ergs^{-1})	location w.r.t. SFMS ^(b)	choice of EM12 template ^(c)
PG0003+199 ϵ	1.5813	20.2029	0.025	43.748	7.222	43.914±0.019	43.213±0.1	0	3
PG0923+129	141.5137	12.7343	0.029	43.081	7.857	43.607±0.004	43.990±0.1	0	2
PG1534+580	233.9682	57.9026	0.030	43.404	7.706	43.518±0.092	43.208±0.1	0	1
PG1310-108	198.2741	-11.1284	0.035	43.277	7.456	43.491±0.046	43.127±0.1	0	1
PG0921+525	141.3036	52.2863	0.035	43.098	6.979	43.729±0.022	43.216±0.1	0	3
PG1501+106	226.0050	10.4378	0.036	43.759	7.989	43.968±0.111	43.608±0.1	0	1
PG1535+547	234.1598	54.5592	0.038	43.580	6.874	43.784±0.093	43.064±0.1	0	3
PG2304+042 $\beta\alpha$	346.7621	4.5492	0.042	43.592	8.270	43.325±0.086	–	–	–
PG1022+519 α	156.3803	51.6763	0.045	43.529	6.911	43.529±0.122	–	–	–
PG1244+026 α	191.6469	2.3691	0.048	43.269	6.640	43.641±0.107	–	–	–
PG1149-110	178.0147	-11.3734	0.049	43.658	7.485	43.728±0.097	43.889±0.1	0	1
PG1119+120	170.4463	11.7384	0.049	43.876	7.281	44.033±0.084	44.061±0.1	1	1
PG0934+013	144.2543	1.0954	0.050	43.357	6.818	43.565±0.104	43.936±0.2	1	1
PG1351+236 α	208.5268	23.4303	0.055	43.681	8.090	43.663±0.051	–	–	–
PG1011-040	153.5862	-4.3112	0.058	43.632	7.095	43.852±0.047	43.895±0.1	1	1
PG1126-041	172.3194	-4.4021	0.060	43.819	7.317	44.452±0.025	44.436±0.1	1	2
PG2130+099	323.1159	10.1387	0.061	44.262	7.684	44.569±0.003	44.316±0.1	1	2
PG0050+124	13.3956	12.6934	0.061	44.296	7.808	44.865±0.004	45.069±0.1	2	1
PG1229+204	188.0150	20.1581	0.064	44.134	7.830	44.091±0.000	43.923±0.1	0	1
PG0844+349	131.9269	34.7512	0.064	43.969	7.396	44.097±0.069	43.694±0.1	0	2
PG0049+171 β	12.9782	17.4329	0.064	43.433	7.843	43.592±0.059	42.868±0.2	0	3
PG1448+273	222.7865	27.1575	0.065	43.986	6.687	43.988±0.051	43.934±0.1	1	1
PG2214+139	334.3011	14.2391	0.067	44.406	8.455	44.410±0.138	43.576±0.1	0	3
PG2209+184	332.9745	18.6972	0.070	43.703	8.164	43.867±0.169	43.839±0.1	0	3
PG1440+356	220.5311	35.4397	0.077	44.218	7.345	44.578±0.086	44.832±0.1	2	2
PG1211+143	183.5736	14.0536	0.085	44.479	7.663	44.750±0.032	43.474±0.1	0	2
PG1426+015	217.2774	1.2851	0.086	44.444	8.540	44.664±0.009	44.456±0.1	1	2
PG1351+640	208.3160	63.7627	0.087	44.393	8.551	44.738±0.099	44.708±0.1	1	1
PG1341+258	205.9864	25.6466	0.087	44.019	7.711	44.033±0.029	43.782±0.1	0	2
PG1411+442	213.4514	44.0039	0.089	44.311	7.867	44.709±0.017	44.028±0.1	0	3
PG0007+106	2.6292	10.9749	0.089	44.404	8.285	44.544±0.057	44.295±0.1	1	2
PG1404+226	211.5912	22.3962	0.098	44.165	7.071	44.104±0.040	43.971±0.1	1	3
PG0804+761	122.7442	76.0451	0.100	44.612	8.203	45.032±0.105	43.799±0.1	0	3
PG1617+175 $\beta\varphi$	245.0470	17.4077	0.114	44.283	8.477	44.643±0.419	42.000±0.3	0	3
PG1415+451	214.2534	44.9351	0.114	44.219	7.721	44.436±0.056	44.394±0.1	1	2
PG1552+085	238.6857	8.3726	0.119	44.432	7.573	44.357±0.071	43.670±0.1	0	3
PG1613+658	243.4882	65.7193	0.129	44.700	8.910	44.999±0.036	45.299±0.1	2	1
PG1435-067	219.5673	-6.9724	0.129	44.388	8.118	44.502±0.070	43.586±0.1	0	3
PG1416-129	214.7659	-13.1791	0.129	44.119	8.387	44.292±0.082	44.103±0.2	0	3
PG1612+261	243.5550	26.0712	0.131	44.425	7.806	44.602±0.114	44.694±0.1	1	1
PG0838+770	131.1888	76.8860	0.131	44.155	7.655	44.451±0.054	44.547±0.1	1	1
PG1626+554 γ	246.9838	55.3754	0.133	44.449	8.327	44.317±0.243	–	–	3
PG1519+226	230.3094	22.4622	0.137	44.102	7.604	44.750±0.049	44.354±0.1	1	3
PG0026+129	7.3071	13.2678	0.142	44.665	7.809	44.678±0.077	43.725±0.1	0	3
PG1114+445 φ	169.2767	44.2259	0.144	44.366	8.243	44.929±0.099	42.000±0.3	0	2
PG1115+407	169.6261	40.4317	0.154	44.208	7.672	44.676±0.005	44.931±0.2	2	3
PG1307+085	197.4458	8.3301	0.155	44.875	8.610	44.732±0.001	44.025±0.1	0	2
PG0052+251	13.7172	25.4275	0.155	44.782	8.581	44.858±0.052	44.558±0.2	1	3
PG1352+183 $\beta\varphi$	208.6487	18.0882	0.158	44.322	8.169	44.586±0.016	42.000±0.3	0	3
PG1001+054	151.0839	5.2168	0.161	44.253	7.653	44.703±0.028	44.073±0.1	0	3

(a) uncorrected for host galaxy contamination which, in our sample, we estimate to be typically ~ 20 per cent.

(b) 0 refers to sources below the SFMS; 1 refers to sources on the SFMS; 2 refers to potential starbursts. For a description for how we determined the three groups we refer the reader to section §4.5.1.

(c) 1 refers to the 25th percentile of the median EM12 template; 2 refers to the median EM12 template; 3 refers to the 75th of the median EM12 template. These have negative, flat and positive gradient in the optical-NIR (see grey and black lines in Figure 2), and are characteristic by $L_{\text{torus}}/L_{5\mu\text{m}} = [4.27, 3.58, 3.18]$ respectively.

ϵ Source missing LL spectral information from *Spitzer*/IRS.

β Upper limit in one or two *Herschel*/PACS bands (70 and $160\mu\text{m}$; with 3σ being the requirement for a detection).

γ Upper limit in all three *Herschel*/PACS bands (with 3σ being the requirement for a detection).

α Bad torus fit.

δ Source with *Herschel*/PACS $160\mu\text{m}$ observation affected by blending with a nearby source.

φ Source showing SF activity consistent with zero upon visual inspection; its $\log L_{\text{SF}}$ was arbitrarily set to 42.0 ± 0.3 .

Table 1. Table 1 continued.

<i>Name</i>	<i>RA</i> (deg)	<i>Dec</i> (deg)	<i>z</i>	$\log L_{5100}^{(a)}$ (ergs^{-1})	$\log M_{\text{BH}}$ (M_{\odot})	$\log L_{5\mu\text{m}}$ (ergs^{-1})	$\log L_{\text{SF}}$ (ergs^{-1})	location w.r.t. SFMS ^(b)	choice of EM12 template ^(c)
PG1402+261	211.3176	25.9261	0.164	44.318	7.613	45.115±0.043	44.964±0.1	2	3
PG0157+001	29.9592	0.3946	0.164	44.671	8.631	45.223±0.210	46.043±0.1	2	1
PG1202+281	181.1755	27.9033	0.165	44.574	8.377	44.697±0.027	44.520±0.1	1	1
PG1048+342	162.9329	33.9907	0.167	44.064	7.823	44.413±0.010	44.174±0.2	1	2
PG1322+659	200.9563	65.6967	0.168	44.508	7.834	44.691±0.034	44.556±0.1	1	2
PG1151+117 ^β	178.4553	11.4751	0.176	44.729	8.478	44.552±0.004	43.709±0.2	0	2
PG1116+215	169.7862	21.3217	0.177	45.126	8.557	45.294±0.121	44.301±0.1	0	3
PG1309+355	198.0740	35.2559	0.184	44.811	8.253	44.959±0.004	44.336±0.1	1	1
PG1012+008	153.7288	0.5604	0.185	44.631	8.346	44.830±0.003	44.631±0.1	1	2
PG0923+201 ^{φβ}	141.4780	19.9014	0.190	44.897	8.036	45.0779±0.177	42.000±0.3	0	3
PG0947+396 ^δ	147.7016	39.4474	0.206	44.657	8.437	44.925±0.011	44.502±0.2	1	2
PG1427+480	217.4295	47.7906	0.221	44.441	7.811	44.707±0.008	44.637±0.1	1	1
PG1121+422 ^γ	171.1633	42.0292	0.234	44.975	8.162	44.709±0.115	–	–	3
PG0953+414	149.2183	41.2562	0.239	45.114	8.361	45.233±0.197	44.081±0.1	0	3
PG1004+130	151.8588	12.8156	0.240	45.232	8.864	45.097±0.033	44.759±0.1	1	1
PG1545+210 ^β	236.9314	20.8713	0.266	45.074	8.878	45.110±0.043	44.283±0.2	0	3
PG1302-102	196.3876	-10.5554	0.286	45.164	8.396	45.335±0.002	45.095±0.1	1	1
PG1700+518	255.3533	51.8222	0.292	45.671	8.753	45.785±0.023	45.723±0.2	2	2
PG1354+213 ^β	209.1367	21.0646	0.300	45.202	8.714	44.983±0.027	44.322±0.2	0	2
PG1100+772	166.0570	76.9828	0.313	45.245	8.961	45.373±0.033	44.915±0.1	1	3
PG2251+113	343.5433	11.6106	0.323	45.625	8.885	45.448±0.107	44.594±0.1	0	3
PG2233+134	339.0320	13.7320	0.325	45.085	7.836	45.244±0.002	44.577±0.1	1	1
PG1216+069 ^{βφ}	184.8372	6.6440	0.334	45.844	9.195	45.257±0.099	42.000±0.3	0	3
PG1048-090 ^{γδ}	162.8747	-9.3028	0.344	45.450	9.096	45.182±0.033	–	–	3
PG1049-006 (= PG1049-005)	162.9643	-0.8549	0.357	44.971	8.729	45.615±0.010	45.611±0.1	2	1
PG1425+267	216.8984	26.5374	0.366	45.453	9.257	45.314±0.011	44.891±0.1	1	1
PG1704+608	256.1724	60.7418	0.371	45.587	9.286	45.762±0.047	45.507±0.1	1	1
PG1512+370	228.6795	36.8473	0.371	45.065	8.872	45.263±0.018	44.708±0.1	1	2
PG0043+039	11.4467	4.1731	0.384	45.412	8.697	45.349±0.018	44.979±0.1	1	3
PG1543+489	236.3760	48.7692	0.400	45.269	8.108	45.696±0.054	45.837±0.1	2	1
PG1103-006 ^{βφ}	166.6324	-0.8812	0.425	45.202	8.924	45.435±0.054	42.000±0.3	0	2
PG2308+098 ^γ	347.8240	10.1376	0.432	45.389	9.237	45.455±0.040	–	–	3
PG0003+158 ^{βφ}	1.4968	16.1636	0.450	45.706	9.021	45.388±0.029	42.000±0.3	0	2
PG2112+059	318.7191	6.1285	0.466	45.710	8.931	45.978±0.093	45.423±0.1	1	3
PG1259+593 ^{βφ}	195.3039	59.0352	0.472	45.572	8.705	45.650±0.143	42.000±0.3	0	3

AKARI. Second, we calculate our mean and median SEDs in a different way compared to S16. We first subtract the SF emission, and then calculate the mean and median spectra after normalising the individual intrinsic AGN SEDs at a chosen wavelength ($\lambda_{\text{rest}} = 20\mu\text{m}$). Below we discuss the implications of this different procedure, and in the Appendix we demonstrate how the choice of method leads to significantly different SEDs. Third, we consider the entire sample of PG quasars (cf. only those with $z < 0.18$ in S16), making the results more applicable to the overall population. Lastly, the SF template we consider here are from CE01 while those used by S16 are the Dale & Helou (2002, hereafter DH02) templates. To quantify the impact of this difference on our results, we repeated our analysis with the DH02 SF templates. We recovered a consistent result (shown in the Appendix) as when we use the CE01 library, thus the choice of SF templates does not significantly affect the findings discussed below. When following the subtraction procedure outlined above, for 11 sources we are left with SF-subtracted SEDs that are negative in any of the *Herschel*/PACS bands. For these we repeat the SF subtraction after replacing their previously considered L_{SF} with the lower limit ($L_{\text{SF}} - \delta L_{\text{SF}}$), on this luminosity, taken from the relevant work (ours/S16).

In Figure 5 we show the individual SF-subtracted SEDs for our sample of PG QSOs (grey lines), normalised to $20\mu\text{m}$, and the resulting median intrinsic AGN SED (solid magenta line). It is apparent that, when using the PAHs-based SF luminosities, there are many SEDs that are considerably colder than the EM12 SEDs, as is the resulting *median*. This (which

we take to be the best representation of the population in this exercise) is also considerably below the *mean* SED presented in S16 (green line). This has important consequences for the characterization of the entire population, and the suggestion that (SF-unrelated) dust is present at large distances from the BH. Quantitative estimates for the contribution of such large-scale dust to the mean FIR luminosity are given in § 4.4. In Figure 5 we also show the median intrinsic AGN SED (dashed magenta line) we would obtain if we only considered those PG quasars that are not upper limits in the PAH-based SF luminosities of Shi et al. (2007). This line indicates that even when we consider those PG quasars which have the more robust SF luminosities we obtain a median intrinsic AGN SED that is consistent with that of the full sample.

We then considered those 12 sources that represent the top 16 per cent with the largest difference between their normalised SF-subtracted $70\mu\text{m}$ luminosity and that of the PAH-based median intrinsic AGN SED (“top 1 σ ” sources hereafter). Their PAH-based median intrinsic AGN SED is given by the purple line, and is significantly different from all the other SEDs shown in this figure.

We also investigated whether the different SED shapes derived with PAH-based luminosities were driven by SF or torus luminosity, and the results are summarized in Figure 6. Here we show the ratio between the SF-subtracted luminosity measured at $70\mu\text{m}$ and that measured at $12\mu\text{m}$ (i.e. a proxy for shape in this region of the SED) as a

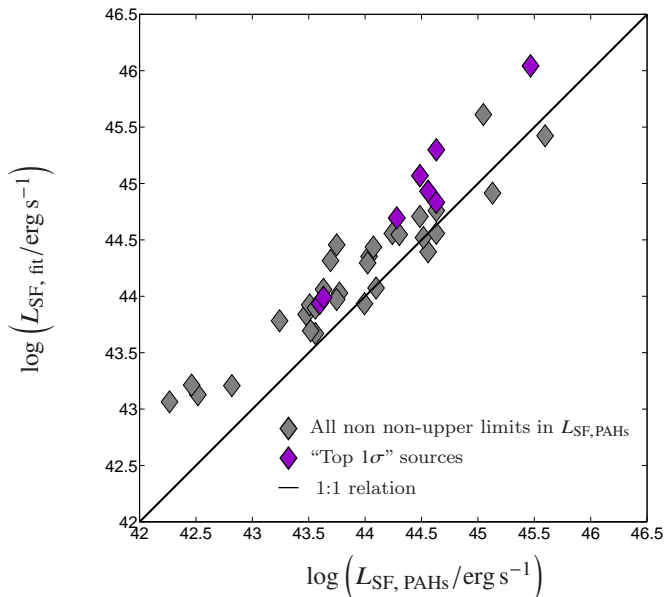


Figure 4. Comparison of star formation luminosities as measured from aromatic features, along the x-axis, and from our SED fitting, along the y-axis, for PGs that are not upper limits in $L_{\text{SF, PAHs}}$ (Shi et al. 2007). The solid line is the 1:1 relation, while the purple points highlight those sources that we have defined as “top 1σ ” (§3.3). For most sources, $L_{\text{SF, fit}}$ is larger than the corresponding $L_{\text{SF, PAHs}}$. It also appears that the majority of the “top 1σ ” sources lies in the region where $L_{\text{SF, fit}}$ is ~ 3 times $L_{\text{SF, PAHs}}$.

function of SF luminosity from our SED fitting (left-hand panel), SF luminosity from PAHs (middle panel), and torus luminosity (right panel). It is clear that in all three panels there is no correlation for the general population, and we can therefore conclude that the differences in shape do not depend on L_{SF} and $L_{\text{AGN}} (\propto L_{5\mu\text{m}})$. On the other hand, if we focus on the “top 1σ ” sources, highlighted by purple squares, they mostly appear at the high end of the L_{SF} and $L_{5\mu\text{m}}$ distributions.

We note that for the results discussed in §4.3 and §4.5 we assume the EM12 template, as explained below and in the relevant sections.

4 DISCUSSION

Thus far we have compared and contrasted the results obtained when employing different methods to estimate the SF activity and the typical intrinsic AGN SED in low redshift AGNs. We found that the consideration of aromatic features yields star formation luminosities that are consistently smaller than those obtained from MIR-FIR SED fitting. Furthermore, we found that the methodology followed to constrain the typical FIR shape of the intrinsic AGN SED in PG quasars strongly impacts on the outcome.

In this section we discuss and interpret our findings. We revisit the issue of “intrinsic AGN SED” and we explore the properties of the cooler dust, referred to here as “large-scale AGN-heated dust” (see §4.4 on the possibility of this dust

being part of the torus/being SF-related), which were identified when considering PAH-based SF luminosities. Furthermore we also want to investigate the torus covering factor and the instantaneous relative growth rate of BHs and their host galaxies, when assuming the EM12 SED to describe the torus and the NLR emission in the considered quasars. Part of the reason why we consider the EM12 SED, rather than that obtained in §3.3, is that we believe it to be more robust because determined on a larger sample. Our choice, however, is further motivated in the remainder of this section.

4.1 Comparison of the PAH-based and SED-fitting-based SF luminosities

The SF estimates from SED fitting, assuming the EM12 SED, are systematically larger than those obtained from the PAH-based method (see Figure 4). It is, however, hard to conclusively determine which method is more reliable. On the one hand, fitting SF templates using *Herschel* data is far superior in terms of data quality, and does not suffer from the uncertainties due to fitting the PAH spectrum and the large, intrinsic, luminosity-dependent scatter due to the conversion from PAH luminosity to SF luminosity. On the other hand, the PAH-based method is independent of the assumed torus SED.

Finally we compared our SED fitting-based SF luminosities with those calculated by Petric et al. (2015, their Table 4). Similarly to the current study, they also considered the full sample of PG quasars and estimated their SFR from FIR *Herschel* photometry. We find that, when considering their $L_{\text{FIR}[40-500\mu\text{m}]}$, they are consistent with a typical difference of 0.07 dex. We note that Petric et al. (2015) also finds SF luminosities that are approximately a factor of 2 larger than those quoted in Shi et al. (2007).

4.2 Re-visiting the intrinsic AGN SED

4.2.1 Observational constraints on the intrinsic AGN SED

Figure 7 shows the comparison of the EM12 template (median), the S16 mean intrinsic AGN template and the median intrinsic AGN SED identified in this work, to the *Herschel* 3σ upper limits from the current work (left panel) and those presented in Figure 7 in Netzer et al. (2016, right panel). Here we only consider FIR upper limits as these are the best candidates for cases where the FIR emission is least contaminated by SF activity, thus being AGN-dominated. As previously mentioned, among the PG QSOs, there are 4 upper limits in all three *Herschel*/PACS bands (~ 5 per cent of the total), and 12 upper limits (~ 14 per cent of the total) in one or two *Herschel*/PACS bands (see Table 1). The EM12 template is consistent with all 3σ upper limits, both at high and low redshift. In contrast ~ 80 per cent of the *Herschel*/PACS 3σ upper limits in the PG sample, and ~ 40 per cent of the *Herschel*/SPIRE 3σ upper limits from Netzer et al. (2016), fall below the mean S16 SED. For the PG sample, we would expect a smaller fraction of the upper limits to fall below the S16 mean, if this SED indeed represented the mean population properties. This is most noticeable in the range $\lambda_{\text{rest}} = 70 - 120\mu\text{m}$, where nearly all 3σ upper limits fall below the S16 line. This contradiction is even more apparent in the high-redshift sample since, if the

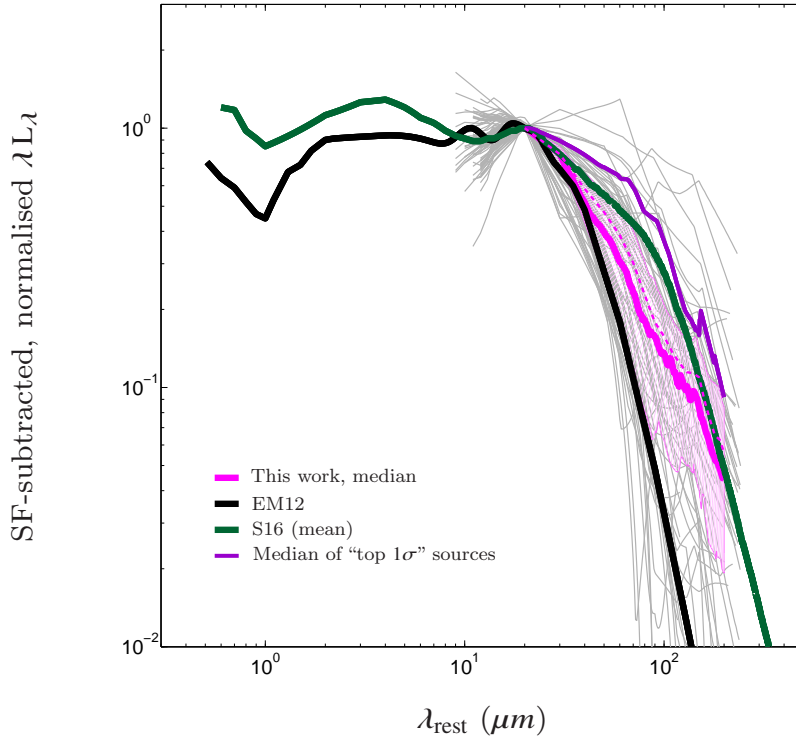


Figure 5. Normalised SF-subtracted SEDs for our sample of PG QSOs (grey lines) when using the PAH-based method (updated where relevant as described in §3.3). The black and green lines correspond to EM12 and S16 intrinsic AGN SEDs, respectively. The solid magenta line is the median PAH-based intrinsic AGN SED obtained in the current work. The purple line is the intrinsic AGN SED obtained when considering those 12 sources that we defined as “top 1σ ” in §3.3, and that we discuss in §4.2. The dashed magenta line corresponds to the median intrinsic AGN SED we obtain when only considering PG quasars that are not upper limits in the PAH-based SF luminosities of Shi et al. (2007).

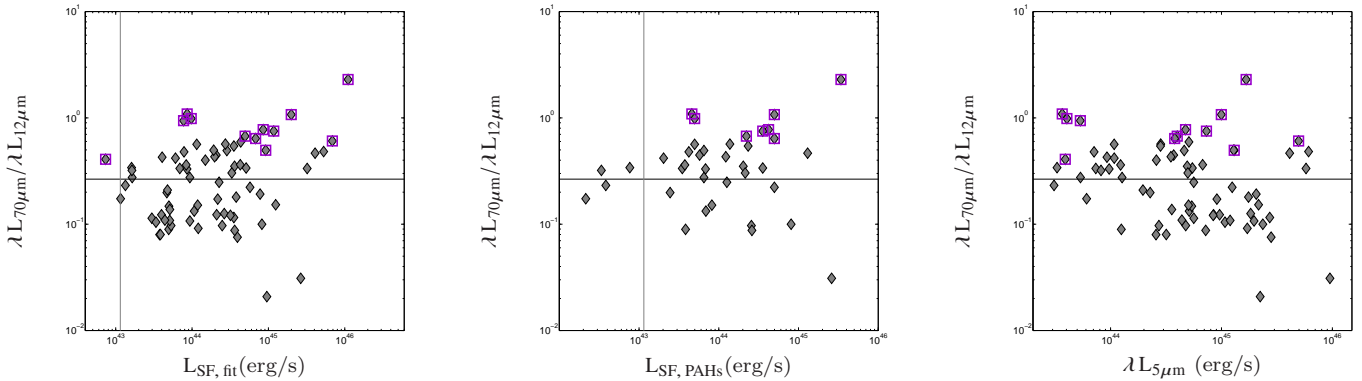


Figure 6. Ratio of the SF-subtracted luminosity measured at $70\mu\text{m}$ and that measured at $12\mu\text{m}$ for our PG QSOs, as a function of SF and AGN luminosities. The purple squares highlight the “top 1σ ” sources. The left panel considers the SF estimated from our SED fitting that assumes the EM12 SEDs, while the middle panel that from Shi et al. (2007), based on PAHs, for non-upper limits only and updated, if required, as previously mentioned (§3.3). No significant correlation appears between the shape of the intrinsic AGN SED of the full population, and the three quantities considered. The “top 1σ ” sources, however, mostly appear at the high end of the distributions. In the left panel the vertical line indicates the SF luminosity corresponding to star formation rate $SFR = 0.1 M_{\odot} \text{yr}^{-1}$.

S16 mean SED were representative of this population, all sources below the line would instead be within the *Herschel* detection limit, appearing as real *Herschel* detections rather than upper limits.

Moreover, the median stacks obtained from the $250\mu\text{m}$

upper limits in Netzer et al. (2016, 66 sources) that are shown in the diagram, mark the locations that divide the population in equal parts (i.e. 50 per cent of the luminosities in these undetected sources should lie below these stacks). This is in clear contradiction with the assumption that the

mean intrinsic AGN SED proposed by S16 represents this population since, in such a case, the calculated stacks (median or mean) would lie close to the S16 SED rather than a factor of ~ 3 below. On the other hand, the median PAH-based intrinsic SED calculated for the PG sample in the current work lie much closer to the high redshift median stacks, as should be the case if the “typical” intrinsic SED shape is independent of AGN luminosity.

All the above considerations suggest that there is no simple way to distinguish between EM12 SED and the median, PAH-based SED obtained here. Conversely, even allowing for the intrinsic scatter expected around an averaged quantity, the mean S16 SED seems to be in conflict with many observations, most noticeable involving *Herschel* upper limits. As shown in the Appendix, we believe that the mean S16 SED represents a few more luminous sources rather than the entire population.

4.2.2 Large-scale dust and its impact on the estimate of SF luminosities

Figure 5 also unveils that some SEDs obtained with the PAH-based method lie far above the median and the mean SEDs of the sample. As previously mentioned, the purple line represents the median intrinsic AGN SED obtained when considering “top 1σ ” sources (as defined in §3.3). We also show this median SED in the right panel of Figure 8. If the PAH-based method provides an accurate way to derive the intrinsic AGN-heated dust emission, these sources may have the strongest contribution from the potential large-scale dust component. *Alternatively*, these sources could be those with the least reliable PAH-based SF estimates. Figure 4 shows that these sources (marked in purple) clearly lie where the discrepancy in the SF measurement between the two methods is large. We cannot, however, say whether this deviation from the median is due to the subtraction of an erroneous amount of PAH-determined SF, or because of extra contribution by large-scale AGN-heated dust which invalidates the consideration of the EM12 template.

The left panel of Figure 8 shows the PAH-based median intrinsic AGN SED, and its 25th – 75th percentiles range (pink hatching). The dark blue line in this figure was obtained by summing the median EM12 SED to a modified blackbody ($\beta = 1.5$) with a temperature of $T_{\text{cold dust}} = 25.5$ K. While this provides the best single temperature fit (through χ^2 minimisation), we caution that it should not be considered as the ultimate value given the large associated uncertainties. In fact, the excess over the EM12 SED can be fitted, reasonably well, with a range of temperatures, from 20 K to about 30 K. In the right panel of Figure 8 we show, in purple, the median intrinsic AGN SED obtained when considering the “top 1σ ” sources, with the corresponding 25th – 75th percentiles (pink hatching). In this case, there is no way to fit the difference between this SED and EM12 with a single modified blackbody. Upon experimenting we find that the required range of temperatures is between 10 K and 60 K. Given the large uncertainties associated with the PAH-based method, we choose not to attempt a full fit of this difference, and only to measure the differences in the total emitted radiation (see §4.4). We also repeated this analysis replacing the set of modified blackbodies with the

CE01 SF templates. We found that we can fit the residual emission with a single SF template, both for the SED based on the full sample and that based on the “top 1σ ” sources. Although the resulting additional SF is within the uncertainties accompanying the best fitting SF luminosities, it may be indicative of star formation that was not properly captured by the PAH-based estimates (and consequently by the subtraction).

Finally, we estimated the uncertainties in the measured SF luminosities introduced by the various intrinsic AGN SEDs, as a function of AGN luminosity. These numbers can also be used to estimate the contribution of cold, large-scale AGN dust, if real, to the total SF luminosity. The natural way to do such a test is to fix L_{SF} and then compute the ratio of SF luminosity and AGN-heated dust luminosity at a pre-chosen wavelength, for every considered value of L_{torus} . Here we chose this fiducial wavelength to be $70\mu\text{m}$ which is close to the peak in νL_{ν} of most SF templates used in this work. We examined two cases, the EM12 SED and the new PAH-based median intrinsic AGN SED obtained in this work. For illustration, we fix the SFR to be $10M_{\odot}/\text{yr}$ and show the results for various ratios of $L_{\text{torus}}/L_{\text{SF}}$ in Table 2. We note that the consideration of different SF SEDs, other than that arbitrarily picked here, would yield different numbers. The differences, however, are minor and would not impact on the main conclusions of this test. The uncertainty on L_{SF} listed in the table are calculated assuming no subtraction of the AGN contribution at $70\mu\text{m}$. As shown in the table, for the EM12 SED, significant uncertainties, approaching a factor 2, require $L_{\text{torus}}/L_{\text{SF}} > 20$. For the new PAH-based median intrinsic AGN SED, this number is $L_{\text{torus}}/L_{\text{SF}} \sim 10 - 20$. Thus, the SFR uncertainties are small unless $L_{\text{AGN}} \gg L_{\text{SF}}$. These numbers are very different from those presented in S16, where they conclude that the intrinsic AGN SED can be neglected when the observed total host luminosity (SF+AGN contribution) at $60\mu\text{m}$ is twice the AGN luminosity at 5100. The results of our test show that the original $L_{\text{SF}} - L_{\text{AGN}}$ correlation presented in Rosario et al. (2012, their Figure 4) is still valid, unlike what stated by S16 (their Figure 16).

4.3 Torus covering factor

Although it does not constitute a main point of our work, we investigated the covering factor of PG QSOs as they are a significantly more complete sample than others previously considered in the literature for this matter. We follow the methods and discussion in Netzer (2015) and Netzer et al. (2016), and consider the torus+NLR component based on the chosen EM12 template. After dividing our sample in 5 equally spaced L_{AGN} bins we find that the median covering factor for the anisotropic case ($b = 0$ in Equation 3 from Netzer et al. 2016) varies between ~ 0.3 and ~ 0.4 (with a typical error of ~ 0.07) across the 5 AGN luminosity bins. For the isotropic case ($b = 1$ in Equation 3 from Netzer et al. 2016) we find the median covering factor to range between ~ 0.4 and ~ 0.6 (with a typical error of ~ 0.2) across the considered AGN luminosity bins. We also find no statistically significant trend for the change of covering factor with AGN luminosity, confirming the findings of Mateos et al. (2016, 2017), Netzer et al. (2016) and Stalevski et al. (2016).

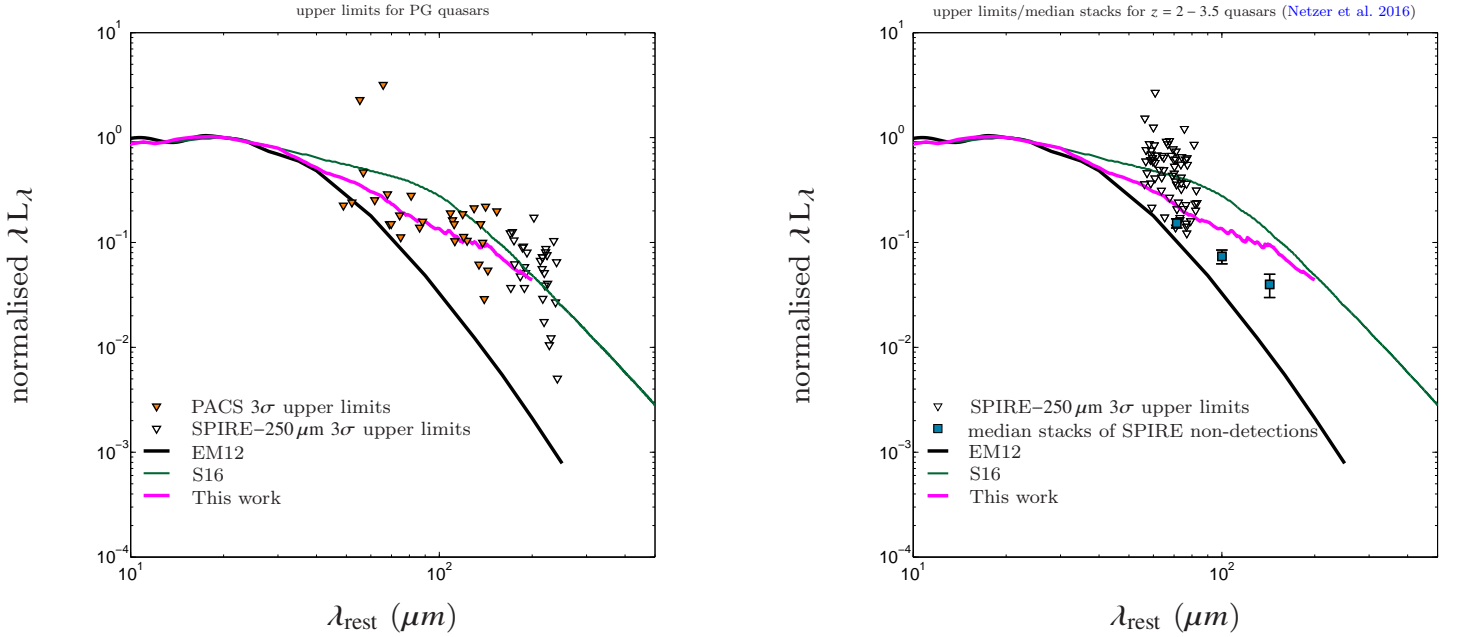


Figure 7. **Left panel.** Zoom-in on the long wavelength region ($\lambda_{\text{rest}} > 10\mu\text{m}$) of the 3 intrinsic AGN SEDs considered in this work. The triangles represent *Herschel*/PACS and SPIRE 3σ upper limits for our PG QSOs. Approximately 80 per cent of the *Herschel*/PACS upper limits lie below the S16 (mean) intrinsic torus SED (cf. 50 per cent below the median intrinsic AGN SED identified in the current work). **Right panel.** The lines have the same meaning as the adjacent panel, however here the triangles represent *Herschel*/SPIRE $250\mu\text{m}$ 3σ upper limits of the $z = 2-3.5$ Netzer et al. (2016) sample. The squares are median stacks of the *Herschel*/SPIRE non-detection for the same sample. In this case ~ 40 per cent of the triangles lie below the S16 SED and, the latter is significantly above the stacked points.

$L_{\text{torus}}/L_{\text{SF}}$	$L_{\text{SF } 70\mu\text{m}}/L_{\text{EM12 } 70\mu\text{m}}$	L_{SF} uncertainty EM12 no torus subtraction	L_{SF} uncertainty PG median no AGN-dust subtraction
1	18.7	5%	10%
5	3.74	21%	36%
10	1.87	36%	53%
20	0.93	52%	69%
30	0.62	62%	77%
50	0.37	73%	85%

Table 2. Uncertainty on SF luminosity due to AGN-heated dust for various assumptions about the dust SED. EM12 is the Mor & Netzer (2012) SED (torus+NLR dust only). For this SED, $L_{\text{torus}} = 30.5 \times L_{70\mu\text{m}}$. “PG median” is the median SED derived in this work using PAH-based SF luminosities (see 3.3). At $70\mu\text{m}$, this SED is a factor of ~ 2.1 more luminous than the EM12 SED. For the PG quasar sample $L_{\text{AGN}} \approx 2 \times L_{\text{torus}}$. The uncertainties are calculated at $70\mu\text{m}$ and are assumed to be also the uncertainties on the total SFR. We assume no subtraction of the AGN-dust contribution at $70\mu\text{m}$. The numbers in the table can also be used to estimate the $70\mu\text{m}$ emission by extended, AGN-heated dust (if real) relative to the SF emission at this wavelength. In our sample the median $L_{\text{SF } 70\mu\text{m}}/L_{\text{EM12 } 70\mu\text{m}}$ is ~ 2.6 .

Lastly we report a lack of correlation between covering factor and Eddington ratio.

We emphasize that the results mentioned here are independent of the choice of intrinsic AGN SED (EM12 vs. the PAH-based median identified in §3.3). As we show in the next section, the difference between the integrated EM12 luminosity and the integrated PAH-based template luminosity is negligible.

4.4 Non-torus dust: temperature, covering factor and location

Here we estimate the covering factor of the potential additional, colder dust component (see §4.2.2 and Figures 5, 8) relative to the covering factor of the torus+NLR emission. We do this by simply comparing the integrated luminosity of the PAH-based median intrinsic AGN SED identified in this work ($L_{\text{cold dust}}$) to that of the EM12 SED ($L_{\text{torus+NLR dust}}$),

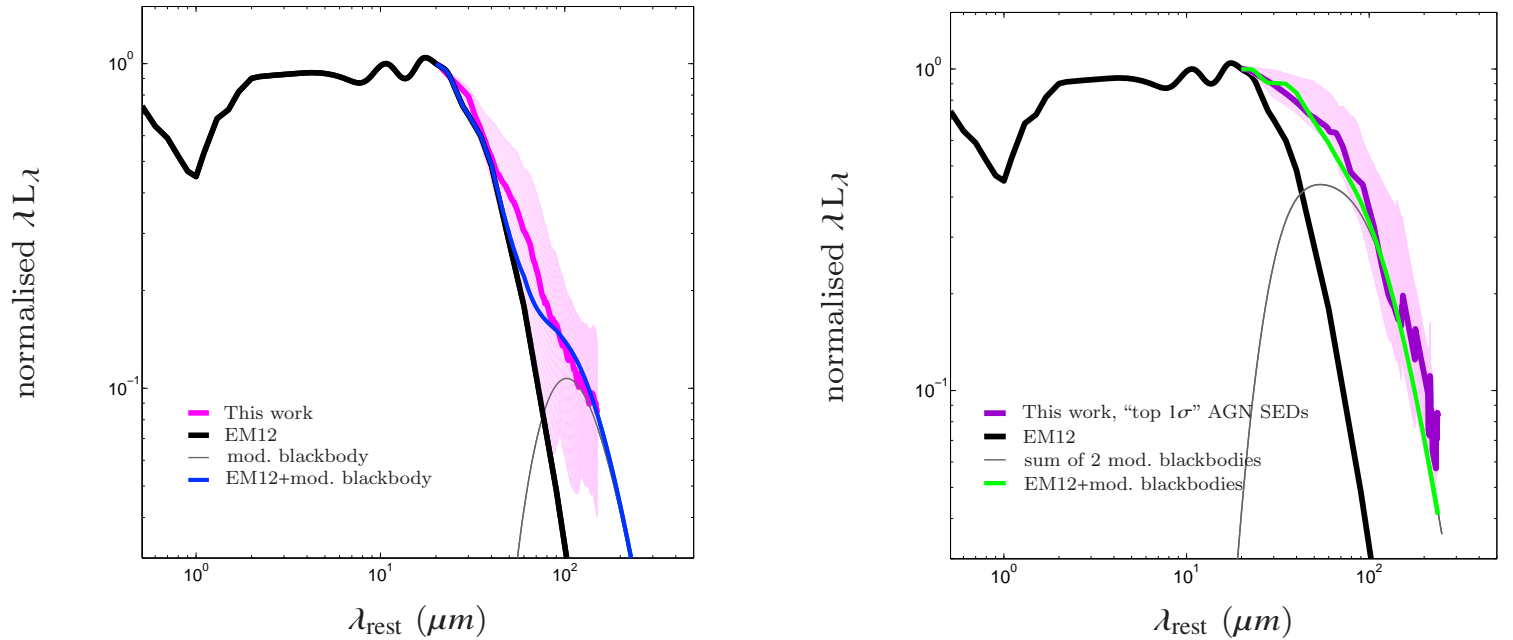


Figure 8. **Left panel.** In magenta we show the median intrinsic AGN SED as found in this work (with pink hatching representing the 25th and 75th percentiles) when considering our PG sample. In blue we show, for illustration only, the composite SED obtained by summing a modified blackbody with temperature of $T_{\text{cold dust}} = 25.5 \text{ K}$ and $\beta = 1.5$ (grey line) to the EM12 median intrinsic AGN SED (black line). **Right panel.** The black line has the same meaning as in the adjacent panel, while the purple line is the median intrinsic AGN SED obtained when only considering the 12 “top 1 σ ” sources (see §3.3). In this case one modified blackbody ($\beta = 1.5$) does not provide a satisfactory fit, and here we show the sum of two modified blackbodies (grey line) with temperatures $T = 29 \text{ K}$ and $T = 60 \text{ K}$ for illustration.

which represents emission from the torus and the NLR only. We do so in two wavelength ranges: $\lambda_{\text{rest}} \sim 1 - 243 \mu\text{m}$ and $\lambda_{\text{rest}} \sim 20 - 243 \mu\text{m}$. The wider wavelength range provides us with information about the “full” covering factor, while the narrower range gives us an idea of the relative contributions in the region where the extra cold dust component is more noticeable. We note that short-ward of $20 \mu\text{m}$ we assume the new PAH-based intrinsic SED to be identical to the median EM12. Here we do not consider the case of an-isotropic dust emission, since the large-scale, colder dust is most likely optically thin. For the PAH-based median SED of the entire sample, we find $L_{\text{cold dust}}/L_{\text{torus+NLR dust}} = 1.26$ in the narrower wavelength range, and $L_{\text{cold dust}}/L_{\text{torus+NLR dust}} = 1.06$ for the wider wavelength range. For comparison these numbers are ~ 58 per cent and ~ 12 per cent when considering the S16 mean SED in place of our median, PAH-based SED. For the group of 12 sources with potentially the largest contribution from the cold dust component (i.e. the “top 1 σ ” sources), we have $L_{\text{cold dust}}/L_{\text{torus+NLR dust}} = 1.90$ for the narrower range and $L_{\text{cold dust}}/L_{\text{torus+NLR dust}} = 1.19$ in the wider range. The contributions with respect to the bolometric AGN luminosity is about 50 per cent of the contributions calculated above because the torus covering factor is $\sim 1/2$. This means that in the majority of the sources the cold dust covering factor is of order $\sim 2 - 3$ per cent, which we consider consistent with zero. We note that this number is based on total energy considerations and the geometrical covering factor can

be larger if the dust is optically thin to some of the AGN radiation.

Moreover we can use the derived temperature ($T_{\text{cold dust}}$, §4.2) together with some basic assumption (e.g. the SED of the optically thin dust is well described by a single β), to estimate the distance between the AGN and the extra dust component. The first possibility is optically thin dust, where the distance (r) from an emitting source of energy L_{AGN} is given by the following equation:

$$\frac{r}{pc} = \left(\frac{1500}{T_{\text{cold dust}}} \right)^{\frac{4+\beta}{2}} \left(\frac{L_{\text{AGN}}}{10^{46}} \right)^{\frac{1}{2}}, \quad (2)$$

where $\beta \sim 1.5$. For the median based on the “top 1 σ ” sources we cannot estimate r , as we could not find a satisfactory fit with a single-temperature modified blackbody. On the other hand, for the generic median the temperature is $T \sim 25.5 \text{ K}$ and $L_{\text{AGN}} = 2.3 \times 10^{45} \text{ erg/s}$, yielding $r \sim 35 \text{ kpc}$. We caution that this estimate may not be entirely meaningful because many sources within the full sample do not show a clear extra dust component (see Figure 5). This number ($r = 35 \text{ kpc}$) is very large, and puts the extra-dust component outside the host galaxy of most sources. The recent Symeonidis (2016) work applies the same considerations to the sources from Netzer et al (2016) that are typically 50 times more luminous than our current sample. The corresponding distances in this case are about 7 times larger, i.e. $\sim 245 \text{ kpc}$. Again this is not plausible, as these scales are significantly beyond the

size of any galaxy at these redshifts (e.g. van der Wel et al. 2014).

The second possibility is that the dust is optically thick at some wavelengths, and hence can be located closer to the central AGN. This raises a different issue related to the column density required to produce the extra emission. Rough calculations show that for a gas of solar metallicity with a column density of $N_{\text{H}} \sim 10^{21.3} \text{ cm}^{-2}$, the range of temperatures inside a dust shell, whose location is 4 kpc from a source with $L_{\text{AGN}} = 2 \times 10^{45} \text{ erg/sec}$, is $T = 25 - 45 \text{ K}$ (depending on the gas density and ionizing continuum shape). This results in a spectrum which is not too different from the single temperature SED assumed for optically thin dust. However, this column is large enough to attenuate, considerably, the optical UV continuum of the source, if located along the line of sight. This is not observed in the optical-UV SED of the sources in question. Moreover, if the covering factor of this component is of order a few percent, this gas will produce strong emission lines, of low or high ionization (depending on the density), that can outshine the NLR emission. Regarding the possibility of unusually cold torus dust, energy considerations, combined with the assumed temperature, suggest a minimal radius of approximately 160 pc. Thus, the location and physical properties of the component responsible for the additional dust emission (if any) must be carefully modeled.

Within this context, we note that Baron et al. (2016) recently found evidence for large-scale dust in luminous SDSS type-I AGN, responsible for a typical reddening $E_{\text{B}-\text{V}} \sim 0.08 \text{ mag}$ ($N_{\text{H}} \sim 10^{20.7} \text{ cm}^{-2}$ for a solar metallicity gas). This is roughly in agreement with the necessary additional dust emission but not with the low temperature deduced here.

Finally, we caution that these geometric scale considerations for an AGN-heated cold dust component will not apply if the non-torus cold dust is related to star formation that was not properly captured by the PAH-based SF estimate, as for a PAH to SFR scaling following Lyu & Rieke (2017) rather than Shi et al. (2007). If this were the case, the SF-related dust could be placed at any location in the galaxy that is not directly exposed to AGN radiation, for example in the large solid angle shielded by the torus.

4.5 Black hole and stellar mass growth

In this section we want to investigate how the black hole, and host’s stellar mass grow, in the PG quasars. Specifically we want to compare these growths to those found in other samples, in particular those with higher redshift and significantly more massive BHs. The median BH mass for the PG sample is $M_{\text{BH}} \sim 3 \times 10^8 M_{\odot}$, while the sample on which we will focus for the comparison (i.e. Netzer et al. 2016) is characterised by a typical black hole mass at $z \sim 3$ of $M_{\text{BH}} \sim 10^{10} M_{\odot}$.

4.5.1 L_{SF} vs. L_{AGN}

The topic of L_{SF} vs. L_{AGN} has been considered in many earlier works using several parallel approaches and, hence, showing seemingly different results (see below). This issue has been discussed at length in Netzer et al. (2016) and we refer the reader to their work for more details. Here we only discuss the points most relevant to the current study.

The first important issue is how the sample is selected – either by using its AGN properties (e.g. Netzer 2009; Rosario et al. 2012; Stanley et al. 2015) or its IR properties (e.g. Chen et al. 2013; Delvecchio et al. 2015). Given the combination of colour and flux used for the selection of the PG sample, we only discuss samples selected by their AGN properties (X-ray or optical-UV). The second issue is whether the analysis refers to the mean, median or individual IR luminosities. Samples analyzed by their mean IR (mostly FIR) luminosity give more weight to sources of higher luminosity. On the other hand, flux limited UV or X-ray samples contain many more low luminosity sources, close to the flux limit of the sample.

Using mean observed properties is most useful when studying the cosmic SFR of the entire population. This approach, however, is accompanied by the loss of the information about the distribution of SFR in a certain bin of redshift and L_{AGN} . For example, in the Stanley et al. (2015) sample only 10–20 per cent of the AGNs in a given L_{AGN} bin were individually detected by *Herschel*. Mullaney et al. (2015) also showed that, given a distribution of star formation rates, the use of its linear-mean rather than the individual values can lead to the results being biased by the more luminous outliers. This highlights also another issue: the consideration of median properties vs. mean properties in the analysis. The great advantage of the sample under consideration here is the possibility to use all the above methods: individually measured L_{SF} (for ~ 95 per cent of the sources), and mean L_{SF} and median L_{SF} for the entire sample.

In the top left panel of Figure 9 we show the mean and median star formation luminosities, as found in our sample of PG QSOs (large squares and large diamonds respectively) when assuming the EM12 AGN template. The colour-coding is based on the average redshift of the respective bins, while the grey points show the underlying distribution of individual sources. It is apparent that in our sample there exists a trend between AGN luminosity and SF luminosity. In the same panel, we also show two curves obtained from Rosario et al. (2012), scaled up assuming $L_{\text{SF}} = 2 \times L_{60\mu\text{m}}$. There seem to be a consistent behaviour within the luminosity range where the two works overlap, regardless of whether we consider mean or median SF luminosities for our sample. Finally, in this figure the circles represent the findings of Stanley et al. (2015), within a similar redshift range to that of our sample. This diagram illustrates the steepening of the relationship, from basically no dependence in the SF-dominated region, to a logarithmic slope in the AGN-dominated region.

To test this more quantitatively, we focus on individual sources, avoiding all methods based on mean properties. We want to investigate whether the relationship between L_{SF} and L_{AGN} depends on the SF properties of the host, i.e. the location of the host with respect to the SF main sequence (SFMS). This requires information about M_{\star} for all the host galaxies. In our sample of type-I AGN, we do not have measurements of M_{\star} . We can, however, use standard low redshift scaling relations to get an approximation for the total stellar mass, starting from the measured M_{BH} . Such relations have been investigated in numerous papers, e.g. Kormendy & Ho (2013); Läscher et al. (2014a,b); Reines & Volonteri (2015); Shankar et al. (2016). There are large differences between the various studies linked to galaxy morphology (i.e. the

differences between total mass and bulge mass in early- and late-type galaxies), the method used to measure the BH mass (e.g. direct dynamical measurements, σ^* -based measurements, L_K -based measurements, reverberation mapping-based measurements, BHs in megamasers), and the sample selection method. A clear trend emerging from all such studies is that M_*/M_{BH} increases with decreasing BH mass (compare e.g. the Reines & Volonteri 2015 ratio of ~ 4000 for $10^7 < M_{\text{BH}} < 10^8 M_\odot$ with ratios of 200–400 found in systems with $M_{\text{BH}} \sim 10^9 M_\odot$ e.g. Kormendy & Ho 2013). There are, however, large differences between all these results, some of which may be related to the uncertainties in estimating BH mass in systems that are not bulge-dominated. We use a method which is similar to that used in Trakhtenbrot & Netzer (2010). The BH mass is estimated from the $M_{\text{BH}}-\sigma^*$ relationship presented in Kormendy & Ho (2013), and M_* from broad-band SDSS photometry. For the current study, we obtained such measurements for about 20,000 SDSS/DR7 type-II AGNs and fitted them by,

$$\log M_*/M_{\text{BH}} = 3.3 - 0.5 (\log M_{\text{BH}} - 7.5). \quad (3)$$

The numerical values obtained in this way are in agreement with the Reines & Volonteri (2015) and Läsker et al. (2016) for low M_{BH} , and converge to the Kormendy & Ho (2013) ratios for the most massive BHs in our sample, assuming $M_* = (1 - 2) \times M_{\text{bulge}}$. Furthermore, these results in M_*/M_{BH} are similar to those suggested in Greene et al. (2016) for all (43 early type and 24 late type) galaxies in their sample, over the range of M_{BH} considered here. We have also experimented with a simpler relationship (Equation 10 from Kormendy & Ho 2013 assuming $M_* = 2 \times M_{\text{bulge}}$), finding values of M_* which are not significantly different from the previous approximation for the most massive BHs in the sample. While the uncertainties in this simplified approach are large, the above approximation still allows us to constrain some important *average* properties related to SF in the hosts of PG quasars. We therefore take the black hole mass estimates for our sample, obtained as described in §2.2 and listed in Table 1, and use Equation 3 to obtain stellar masses for every PG quasar.

We used our SF luminosities and the assumption that $1 M_\odot/\text{yr} = 1 \times 10^{10} L_\odot$, together with the assigned M_* and the parameterization of the SFMS given in Whitaker et al. (2012), to determine the location of all our PG QSOs with respect to this sequence. We consider sources that are “below the SFMS” those with SFRs which are at least 0.3 dex below the redshift dependent expression given by Whitaker et al. (2012). This yielded 31 objects on, and 37 objects below, the SFMS. There are 9 more sources which we consider to be above the main sequence and potential starbursts. Their SFR is more than 0.5 dex above the line we use to define the SFMS at their redshift. These objects are suspected to be characterised by high density molecular gas which leads to a much higher efficiency in SF, perhaps caused by mergers. The exact definition of the boundaries of the SFMS changes slightly from one study to the next, but this makes no significant difference to the results considered here and those in §4.5.2. The fraction of starbursting hosts found here is considerably larger than that found in large samples of SF galaxies (Rodighiero et al. 2011). This is not surprising given the suspected merger activity in many hosts of PG quasars (e.g. Veilleux et al. 2009). We note that our analysis may not nec-

essarily work correctly on an object by object basis, due to the large uncertainties, yet we can still apply it to investigate average properties of large samples (like that considered here).

The top right panel of Figure 9 shows all PG sources with reliable SF luminosities (77 objects) and the best linear fit calculated by the standard BCES regression procedure (Akritas & Bershady 1996), that takes into account the uncertainties on both variables. For the error on L_{AGN} we have assumed 0.15 dex for all sources. For the error on L_{SF} , we do not allow an uncertainty below 0.1 dex. For some sources, the formal uncertainty is in the range 0.1 – 0.2 dex; to all these we assigned an uncertainty of 0.2 dex. Finally, 8 sources are consistent with no SF with a formal upper limit of $\log(L_{\text{SF}}/\text{erg s}^{-1}) < 42.3$. All these were assigned SFRs corresponding to $\log(L_{\text{SF}}/\text{erg s}^{-1}) = 42.0$ with an uncertainty of 0.3 dex. We calculated the regression for the three sub-samples (on, below and above the SFMS), as well as for the entire sample. The correlations for the entire sample, and for the sources below/above the SFMS, are not significant. This is due to the very large spread in L_{SF} for a given L_{AGN} , caused by objects with negligible SFR, and the small number of sources above the SFMS respectively. On the other hand, the correlation for the objects on the SFMS is highly significant. It is given by $\log L_{\text{SF}} = (0.72 \pm 0.08) \log L_{\text{AGN}} + (11.80 \pm 3.2)$

The correlation of SFMS sources is consistent with that proposed in Netzer (2009) for the population of type-II AGN with $L_{\text{AGN}} > L_{\text{SF}}$ in the SDSS, and with the recent work by Ichikawa et al. (2016). Interestingly, there appears a considerable difference in the $L_{\text{AGN}}-L_{\text{SF}}$ relation between the group of sources on the SFMS and that above the SFMS (that we caution only includes 9 sources). The latter seems to closely follow a 1:1 relation.

While the result of the correlation analysis depend on two well determined quantities, L_{AGN} and L_{SF} , its main uncertainty is the definition of the SFMS group, as this in turn depends on the large error on the stellar mass estimates. The best way to verify the reliability of this part, is to compare our stellar masses with those recently obtained by Zhang et al. (2016) that are well-determined. They investigated the location of PG QSOs on the SFMS with photometrically-determined stellar masses. They report a tentative dependence of the specific SFR (sSFR) on L_{AGN} , with the more luminous AGNs showing higher sSFRs. A direct comparison of their stellar masses to those obtained in our work shows good agreement, with a typical difference of ~ 0.2 dex. The scatter is distributed nearly symmetrically along the 1:1 line, showing no evidence for systematics in our estimates. We also note that the consideration of stellar masses based on alternative scaling relations (e.g. Kormendy & Ho 2013; Reines & Volonteri 2015) yields a less good agreement in the comparison to the Zhang et al. (2016) photometrically-determined stellar masses. This is further support that our stellar mass estimates, although not necessarily exact on a source by source basis, give a good representation for the typical properties of the AGN population.

When inspecting Figure 9, it is interesting to note some real differences between our UV-selected sample and several X-ray selected samples, like those presented by Rosario et al. (2012), Stanley et al. (2015) and Shimizu et al. (2016). The

former selection method (UV-selected) tends to pick only AGN-dominated sources while the latter (X-ray selected) contain many SF-dominated objects. In general, the X-ray selected samples reach lower AGN luminosity and also lower SFRs. In addition some of the samples provide only mean SFRs, neglecting the location of individual sources in the $L_{\text{AGN}} - L_{\text{SF}}$ plane. Nonetheless some of the differences, especially the lack of rise of L_{SF} with L_{AGN} at low L_{AGN} seen in several X-ray selected samples, seem to be in conflict with the properties of the PG QSO sample.

For completion, we show in the bottom panel of Figure 9 the relationship between L_{SF} estimates from the PAH-based method and L_{AGN} . For clarity, we only plot those sources for which PAH-derived star formation luminosities are not upper limits. The same behaviour of L_{SF} and L_{AGN} is present regardless of the method used to measure SF luminosities. We consider this result less meaningful than that shown in the top left panel of Figure 9, since ~ 50 per cent of the sources could not be used (because upper limits) and hence the sample cannot be considered “complete”.

Finally we note that very recently Shimizu et al. (2016) reported the lack of a correlation for $L_{\text{SF}} - L_{\text{AGN}}$, in a large sample of local X-ray selected AGNs, from the *Swift Burst Alert Telescope* (BAT) 58 month catalogue. After obtaining the full data for their Table 1, and applying the bolometric correction factor they suggest ($L_{\text{AGN}} = 10.5 \times L_{14-195\text{keV}}$), we find a significant overlap for approximately half of the luminosity range covered by the PG quasars. The lack of correlation remains also when we only consider those BAT sources which are AGN-dominated. We suggest two possible reasons for the observed differences. First, having more AGNs with high L_{SF} and low L_{AGN} in the Shimizu et al. (2016) sample, and second the much fewer high L_{AGN} sources ($L_{\text{AGN}} > 2 \times 10^{45}$) in the Shimizu et al. (2016) sample. These are indeed the ones mostly driving the correlation observed in the current work.

4.5.2 SFR/BHAR across cosmic time

The ratio SFR/BHAR can be interpreted as the relative “instantaneous growth rate” of the stellar and BH mass. The term “instantaneous” is correct for the AGN but may be misleading for the SFR. The FIR radiation we measure is emitted by dust which is heated by stars of different ages, occasionally without any on-going star formation. It reflects the average SFR over a period of ~ 100 Myr. Nevertheless, this is an appropriate terminology when comparing to the entire SF history of the galaxy. For $L_{\text{AGN}} = L_{\text{SF}}$, and for mass to radiation conversion efficiency $\eta = 0.1$, SFR/BHAR is ~ 140 . If the ratio does not change with time, and if the duty cycles of SF and BH accretion (the fractions of time the processes are “on”) are identical, at the end of the process we would expect $M_*/M_{\text{BH}} = \text{SFR}/\text{BHAR}$. At low redshift, the duty cycles for SF and BH accretion are very different, as evident, for example, by the much larger number of high mass star-forming galaxies compared to the numbers of luminous AGNs. This means that in the local Universe, the accumulation of stellar mass during the time the BH is active is only a small fraction of the final stellar mass. A rough estimate of the mean relative duty cycle of the two processes is given by $(M_*/M_{\text{BH}})/(\text{SFR}/\text{BHAR})$. This is a ratio we can determine,

with large uncertainty, using the values of M_* obtained as described in § 4.5.1.

We now proceed to contrasting the low redshift PG quasars, and the higher redshift, highest luminosity $z = 2 - 3.5$ AGNs in the Netzer et al. (2016) sample. We emphasize that we do not aim to evolutionally link these two samples, but rather to compare them in order to learn more about the stellar mass and BH mass growth for BHs of different masses. To facilitate this comparison, we note that the median of M_*/M_{BH} in the PG quasar sample is ~ 485 . On the other hand, the high redshift sample contains the most massive BHs at those epochs, that are probably on their way to also become the most massive BHs in the local Universe. Their mean M_{BH} is unknown, but was estimated by Netzer et al. (2016) to be $\sim 10^{9.5-10} M_{\odot}$. From Kormendy & Ho (2013) we find that the hosts of such BHs in the local Universe are large elliptical galaxies and hence we assume $M_* = M_{\text{bulge}}$. For these sources we therefore estimate $M_*/M_{\text{BH}} \approx 100$.

Figure 10 shows the distribution of SFR/BHAR across cosmic time for two samples: our PG sample, the and the $z = 2 - 3.5$ sample of Netzer et al. (2016). The PG QSO sample has individual measurements of both BHAR and SFR. As previously mentioned, the high redshift sources were observed by *Herschel*/SPIRE, with 34 detections and 66 upper limits. The individual measurements of the detected sources were used to obtain the grey squares in Figure 10. The 66 upper limits were stacked to obtain a meaningful median flux corresponding to $\text{SFR} \sim 100 M_{\odot}/\text{yr}$. For these objects (shown as blue squares), we used the stack’s L_{SF} value and their individual L_{AGN} , to calculate their SFR/BHAR ratios. As explained in Netzer et al. (2016), some of these sources are probably on the SFMS and some, perhaps the majority, below the SFMS in quenched hosts. We purposely avoid a comparison with those works that do not have individual measurements in L_{SF} but use stacks or mean values (e.g. Stanley et al. 2015) as, in such studies, the spread in SFR/BHAR at a particular redshift cannot be properly explored.

The histogram of SFR/BHAR for PG quasars on and above the SFMS is shown in Figure 11; the median of this ratio is ~ 17 . For the $z = 2 - 3.5$ sample, we consider sources on or above the SFMS to be only the 34 sources detected by *Herschel*; their median SFR/BHAR ratio is ~ 50 .

The distribution of SFR/BHAR for sources on or above the SFMS, combined with the same ratio for the sources in quenched hosts, can be interpreted as the progression of the duty cycles of SF and BH activity along cosmic time, and as a function of BH mass. The explanation adopted here applies *only* to AGNs that are hosted in SF galaxies on and above the SFMS. We compare two epochs: 2 – 3 Gyr after the Big Bang and the local Universe. For the high redshift sources, the estimated $(M_*/M_{\text{BH}})/(\text{SFR}/\text{BHAR})$ ratio is ~ 2 meaning that in the first 2 – 3 Gyr, the most massive BHs were actively growing during about half the time their host galaxies grew by SF. These numbers are consistent with the scenarios discussed in Netzer et al. (2014) and Netzer et al. (2016) for this population. For the local, lower mass objects the situation is very different, since $(M_*/M_{\text{BH}})/(\text{SFR}/\text{BHAR})$ is $\sim 20 - 100$ with a median value of ~ 56 . This would imply that the BHs are actively growing during about 2–5 per cent of the time that their hosts are forming stars on and above

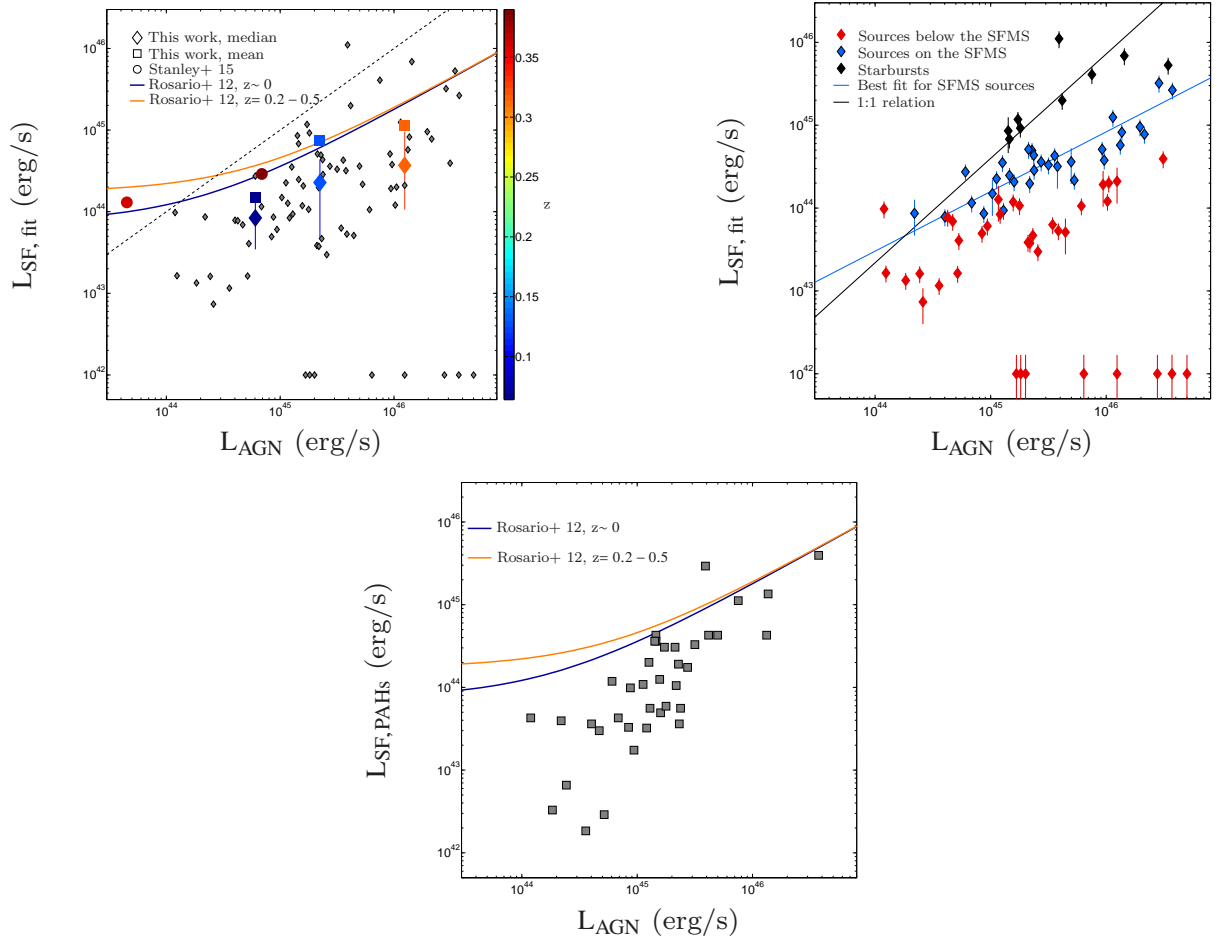


Figure 9. **Top left panel.** Median (diamonds) and mean (squares) L_{SF} in 3 bins of L_{AGN} as found in our sample of PG QSOs, when assuming the EM12 AGN SED. The uncertainties on the median points represent the 25th and 75th percentiles of the distribution in each L_{AGN} bin. The grey points represent the individual sources, while the colour-coding is by redshift and facilitates the comparison with the modified mean relations of Rosario et al. (2012, solid lines, see §4.5.1 for details) and the mean L_{SF} from Stanley et al. (2015, circles). **Top right panel.** L_{SF} vs. L_{AGN} for the PG sample using the EM12-based method to derive SF luminosities. Objects below, on and above the SFMS are colored with green, blue and black respectively. The regression line for the sources on the SFMS is shown with the corresponding colour (see §4.5.1 for details). The black line represents the 1:1 relation and appears to be in good agreement with the $L_{\text{SF}} - L_{\text{AGN}}$ relation observed for the sources above the SFMS. **Bottom panel.** L_{SF} vs. L_{AGN} for SF luminosities based on PAH features. Regardless of the method to estimate SFRs, we find a trend: L_{SF} increases as L_{AGN} increases. For clarity we omitted those sources that are upper limits in Shi et al. (2007).

the SFMS. For example, if a typical SF episode is about 150 Myr, the equivalent BH growth time is about 3 Myr. According to this scenario, we observe the PG quasars during this 3 – 5 per cent of the SF event, which may also be the last event of fast BH growth of this population. We emphasize, again, that all numbers used here are for sources on and above the SFMS. We attribute the very different ratios of $(M_*/M_{\text{BH}})/(\text{SFR}/\text{BHAR})$ at these epochs as due to very different duty cycles. This may be related to either different conditions in the Universe, e.g. the relative fraction of molecular gas in galaxies, or different population properties, particularly BH mass. Finally, we caution that the AGN activity discussed here is not necessarily a single event, and the 5 Myr can be broken into several shorter episodes. Also, there must have been earlier significant SF episodes since the duration and typical SFR measured here are not enough

to explain the stellar mass of these objects. It is very likely that earlier episodes have different SFR/BHAR.

The above explanation depends on several assumptions. On the high luminosity side (i.e. the redshift $z = 2 - 3.5$ sample), we assume that the growth of BHs below the SFMS does not add much to their total mass. A simple scenario involving negative feedback, operating both on SF and BH activity, is consistent with this assumption. On the low luminosity side (i.e. PG QSOs), we assume that the active BHs in SF-dominated systems, like most sources in the Rosario et al. 2012 and Stanley et al. 2015 samples, do not influence the SF in their hosts. The prediction here is that most such systems cannot be distinguished from SF galaxies on the SFMS (for more discussion about the comparison of main sequence SF galaxies and AGN hosts see Santini et al. 2012, Rosario et al. 2013, Hickox et al. 2014 and Mullaney et al. 2015). This is because shallower X-ray

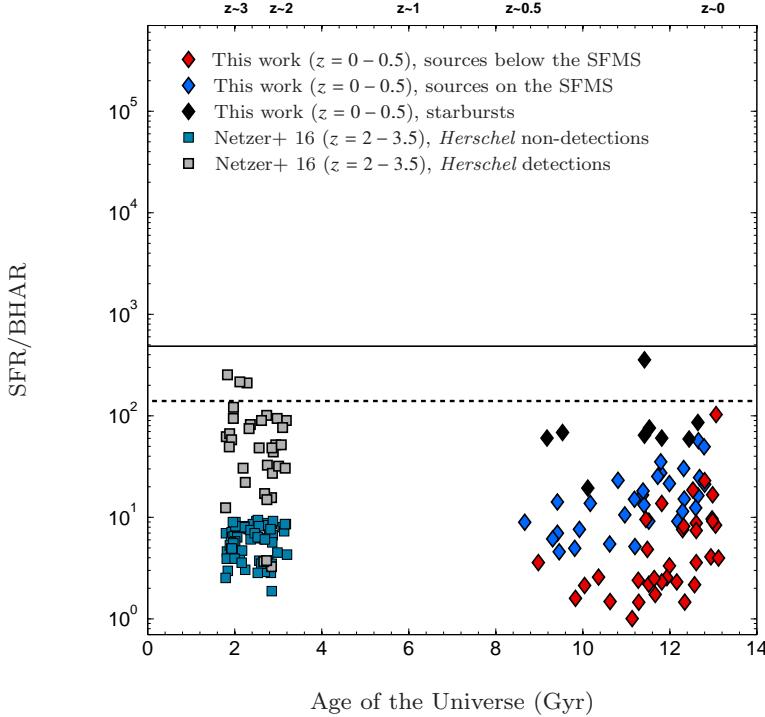


Figure 10. Instantaneous stellar mass to black hole growth rates as a function of cosmic time, for two samples. The blue diamonds represent the PG QSOs on the SFMS. The black diamonds represent PG QSOs that are candidates for starbursts (at least 0.5 dex above the SFMS) and the red diamonds are PG QSOs below the SFMS. The squares represent the sources from Netzer et al. (2016), with *Herschel* detections in grey and *Herschel* non-detections in light blue. The horizontal lines are drawn at $\text{SFR}/\text{BHAR}=140$ (to mark the case where $L_{\text{AGN}} = L_{\text{SF}}$) and 485 (the typical M_*/M_{BH} of the PG QSOs). While we do not trust our division between below/above the SFMS on an individual object’s basis, the well-defined colour segregation for the three groups shown here is confirmation that our division works overall.

surveys would miss the AGN X-ray emission, thus mistakenly classifying a significant fraction of these sources as pure SF galaxies.

There are additional uncertainties and caveats in the above scenario, mostly related to the lack of robust stellar mass measurements and the use of mean (or median) rather than individual properties. This is the case for the $z = 2-3.5$ sample where 2/3 of the sources do not have individual SFR measurements, and none of the sources have stellar mass measurements. In addition, we did not distinguish SFMS galaxies from starburst galaxies, where SF efficiency is high and the stellar mass growth time is shorter. Given the lack of information on individual M_* , we prefer not to discuss these issues any further.

Lastly, we refer to several points in the new Lyu & Rieke (2017) paper that was already mentioned in §1. Their work addresses AGN SED, specifically that proposed in Elvis et al. (1994) and then modified in Xu et al. (2015, ME15 hereafter), which is based on a sample of ~ 50 high luminosity sources. The Lyu & Rieke (2017) analysis suggests ME15 to be the best representation of the intrinsic AGN SED. Our comparison reveals that this SED is consistent with that from EM12 at wavelengths longer than $\sim 2\mu\text{m}$ (see the Appendix). Lyu & Rieke (2017) also suggest that the prescription used by S16 to convert PAH-based luminosities to SF-based luminosities tends to underestimate L_{SF} , again in line with our conclusions. By following the same method as S16 but adopting a different PAH/SF

scaling, Lyu & Rieke (2017) find a PG-based intrinsic AGN SED that significantly differs from that of S16 (their Figure 6). Their conclusions contrast the existence of a significant amount of large-scale, cold AGN heated dust as postulated in S16.

5 CONCLUSIONS

We presented a new analysis of the entire IR spectrum of the PG quasar sample taking advantage of the most updated *Spitzer*/IRS (MIR) and *Herschel* (FIR) observations. The analysis focuses on three major issues: the SED of AGN-heated dust in these sources, the various correlations between L_{SF} and L_{AGN} in this and other AGN samples, and the relative growth rates of BH (BHAR) and stellar mass (SFR). The main results of our work can be summarized as follows:

(i) We compared two different ways of measuring L_{SF} relying on different assumptions. The first is based on fitting *Herschel*/PACS observations using the torus SED presented in Mor & Netzer (2012), after extending it to the FIR (EM12). This method assumes no emission from larger-scale AGN-heated dust. The second method follows the work of S16 where the SFRs are based on PAH luminosity, as measured from *Spitzer*/IRS spectroscopy by Shi et al. (2007). We find that SF luminosities determined from SED fit-

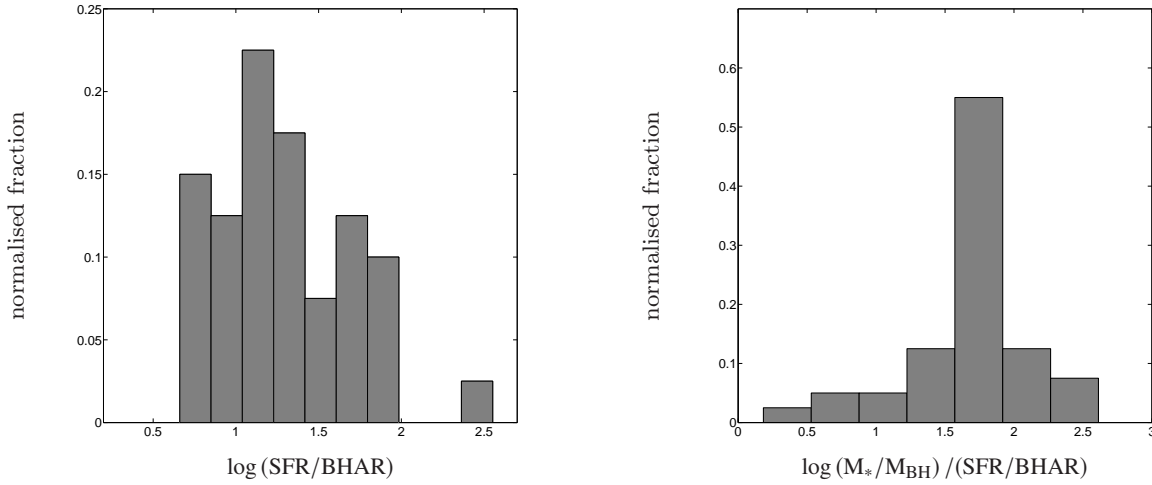


Figure 11. **Left panel.** Histogram of the ratio of SFR to BHAR, for PG QSOs on and above the SFMS; the median ratio is ~ 17 . **Right panel.** Histogram of the “relative duty cycles” of SF and BH activity, defined as $M_*/M_{\text{BH}}/(\text{SFR}/\text{BHAR})$. In this case the median value is ~ 56 , and is significantly different from the value of ~ 2 which is our estimate of this quantity for the high redshift, high luminosity [Netzer et al. \(2016\)](#) sample.

ting are consistently larger than those based on aromatic features (and the specific L_{PAH} to L_{SF} conversion assumed by [Shi et al. 2007](#)). The SF templates matching the PAH-based SF luminosities are then subtracted from the observed MIR-FIR SEDs of the PGs, and the remaining flux is interpreted as the entire (torus and large-scale) dust emission. Our results are at odds with what presented in S16, however there are several important differences between our analysis and theirs. Firstly we used the entire PG sample while S16 used only sources with $z < 0.18$. In addition we used *Herschel*/PACS $70\ \mu\text{m}$ and $100\ \mu\text{m}$, data that were not used by S16. Most importantly, S16 calculated the mean SED of the AGN-heated dust without normalization while we look for the SED shape after normalization at $20\ \mu\text{m}$. The different procedures result in median and mean SEDs that are much weaker and “hotter”, in the FIR, than those proposed by S16. In particular (see Appendix) we show that removing the four AGNs that are most luminous at $70\ \mu\text{m}$ from the S16 sample, reduces the mean S16 SED by a factor of ~ 2 at this wavelength. Our median AGN SED derived with the PAH-based method represents only ~ 6 per cent increase on the total ($1 - 243\ \mu\text{m}$) luminosity of the EM12 torus SED. The increase on the $20 - 243\ \mu\text{m}$ range is ~ 26 per cent. The covering factor required to explain this amount of extra emission by remote AGN-heated dust is only ~ 3 per cent. Moreover, the excess can also be explained by a systematic under-estimation of the SFR by the PAH-based method.

(ii) Assuming that the PAH-based method is correct, we can estimate the properties of the additional AGN-heated dust ($T_{\text{cold dust}}$). For example, for the full sample we find $T_{\text{cold dust}}$ in the range $\sim 20 - 30\ \text{K}$. On the other hand, for the group of 12 sources representing the “top 1σ ” distribution of cold, large-scale dust, we estimate the required temperature range to be $T_{\text{cold dust}} = 10 - 60\ \text{K}$. In both cases, the location of this dust, if optically thin, is outside the host galaxy. Op-

tically thick dust can be located closer to the central source but this requires large column densities and seems to be in conflict with several other observed properties of the sources in the sample. We emphasize, again, that in both these cases, we could find a single SF template that explained the excess emission.

(iii) We obtained rough estimates of M_* using a relation for M_{BH} and M_* determined on a type-II AGN sample from the SDSS. We also verified that these are in reasonable agreement with the recent photometric M_* estimates of [Zhang et al. \(2016\)](#). We used our M_* values to find the location of the host galaxies in the SFR- M_* plane and identify the SF main-sequence (SFMS) for our sample. We examined the correlation between L_{SF} and L_{AGN} and note a significant difference between objects that are on the SFMS, below the SFMS, and above the SFMS (candidates for starbursting hosts). Assuming $L_{\text{AGN}} \propto L_{\text{SF}}^\alpha$, we find $\alpha = 0.72 \pm 0.08$ for objects on the SFMS (31 sources), and no significant correlation for objects below and above the SFMS (37 and 9 sources respectively). There is no correlation for the entire sample because of the sources that are below the SFMS. The potential starbursts, however, appear to cluster along the 1:1 line in the $\log L_{\text{SF}} - \log L_{\text{AGN}}$ plane. We investigated the differences between our results and those found in earlier works, based on X-ray selected samples, like [Rosario et al. \(2012\)](#) and [Stanley et al. \(2015\)](#). We suggest that part of the difference lies in the fact that those samples are dominated by objects that are undetected by *Herschel*. The corresponding studies must, therefore, use stacks or upper limits. This in turn forces the use of mean properties, rather than measured properties of individual sources. However, some of the difference may be real and, thus far, without explanation.

(iv) We examined the relative instantaneous growth rates of BH and stellar mass (SFR/BHAR), and compared them with those measured for the most luminous AGNs at $z =$

2–3.5 (Netzer et al. 2016). For sources hosted by SF galaxies, the comparison of SFR/BHAR with M_*/M_{BH} gives an indication of the relative duty cycles of SF and BH accretion at the two epochs. The differences in relative duty cycles are very large, ranging from about 20–100 in the local Universe to about 2 at redshift $z = 2 - 3.5$. We use these numbers to suggest different scenarios for BH and SF growth rates in systems containing active BHs with a mass of $\sim 3 \times 10^8 M_{\odot}$ in the local Universe, and those containing active BHs with a mass of $\sim 10^{10} M_{\odot}$ at high redshift.

ACKNOWLEDGMENTS

The authors thank Núria Castelló-Mor for helpful discussions, and George Rieke, Taro Shimizu, Benny Trakhtenbrot, David Rosario and Myrto Symenodis for clarifications and important information. They also acknowledge very helpful comments by the anonymous referee. Funding for this work was provided by the Israel Science Foundation grant 284/13. PACS has been developed by a consortium of institutes led by MPE (Germany) and including UVIE (Austria); KUL, CSL, IMEC (Belgium); CEA, OAMP (France); MPIA (Germany); IFSI, OAP/OAT, OAA/CAISMI, LENS, SISSA (Italy); IAC (Spain). This development has been supported by the funding agencies BMVIT (Austria), ESA-PRODEX (Belgium), CEA/CNES (France), DLR (Germany), ASI (Italy), and CICYT/MCYT (Spain).

REFERENCES

- Akritis M. G., Bershadsky M. A., 1996, *ApJ*, **470**, 706
 Baron D., Stern J., Poznanski D., Netzer H., 2016, preprint, ([arXiv:1603.06948](https://arxiv.org/abs/1603.06948))
 Bentz M. C., et al., 2013, *ApJ*, **767**, L49
 Boroson T. A., Green R. F., 1992, *ApJS*, **80**, 109
 Calzetti D., et al., 2007, *ApJ*, **666**, 870
 Chary R., Elbaz D., 2001, *ApJ*, **556**, 562
 Chen C.-T. J., et al., 2013, *ApJ*, **773**, 3
 Dale D. A., Helou G., 2002, *ApJ*, **576**, 159
 Delvecchio I., et al., 2015, *MNRAS*, **449**, 373
 Elbaz D., et al., 2010, *A&A*, **518**, L29
 Elvis M., et al., 1994, *ApJS*, **95**, 1
 Ferrarese L., Merritt D., 2000, *ApJ*, **539**, L9
 Förster Schreiber N. M., Roussel H., Sauvage M., Charmandaris V., 2004, *A&A*, **419**, 501
 Gallimore J. F., et al., 2016, *ApJ*, **829**, L7
 García-Bernete I., et al., 2015, *MNRAS*, **449**, 1309
 García-Burillo S., et al., 2016, *ApJ*, **823**, L12
 Gebhardt K., et al., 2000, *ApJ*, **539**, L13
 Genzel R., et al., 1998, *ApJ*, **498**, 579
 Gillett F. C., Kleinmann D. E., Wright E. L., Capps R. W., 1975, *ApJ*, **198**, L65
 Greene J. E., et al., 2016, *ApJ*, **826**, L32
 Heckman T. M., Kauffmann G., Brinchmann J., Charlot S., Tremonti C., White S. D. M., 2004, *ApJ*, **613**, 109
 Hernán-Caballero A., et al., 2015, *ApJ*, **803**, 109
 Hickox R. C., Mullaney J. R., Alexander D. M., Chen C.-T. J., Civano F. M., Goulding A. D., Hainline K. N., 2014, *ApJ*, **782**, 9
 Hopkins A. M., Beacom J. F., 2006, *ApJ*, **651**, 142
 Ichikawa K., Ricci C., Ueda Y., Matsuoka K., Toba Y., Kawamuro T., Trakhtenbrot B., Koss M. J., 2016, preprint, ([arXiv:1611.09858](https://arxiv.org/abs/1611.09858))
 Jester S., et al., 2005, *AJ*, **130**, 873
 Kormendy J., Ho L. C., 2013, *ARA&A*, **51**, 511
 Läsker R., Ferrarese L., van de Ven G., 2014a, *ApJ*, **780**, 69
 Läsker R., Ferrarese L., van de Ven G., Shankar F., 2014b, *ApJ*, **780**, 70
 Läsker R., Greene J. E., Seth A., van de Ven G., Braatz J. A., Henkel C., Lo K. Y., 2016, *ApJ*, **825**, 3
 Laurent O., Mirabel I. F., Charmandaris V., Gallais P., Madaden S. C., Sauvage M., Vigroux L., Cesarsky C., 2000, *A&A*, **359**, 887
 Lutz D., et al., 2016, *A&A*, **591**, A136
 Lyu J., Rieke G. H., 2017, preprint, ([arXiv:1704.06987](https://arxiv.org/abs/1704.06987))
 Lyu J., Rieke G. H., Shi Y., 2017, *ApJ*, **835**, 257
 Madau P., Dickinson M., 2014, *ARA&A*, **52**, 415
 Madau P., Ferguson H. C., Dickinson M. E., Giavalisco M., Steidel C. C., Fruchter A., 1996, *MNRAS*, **283**, 1388
 Mateos S., et al., 2016, *ApJ*, **819**, 166
 Mateos S., et al., 2017, preprint, ([arXiv:1705.04323](https://arxiv.org/abs/1705.04323))
 Meléndez M., Mushotzky R. F., Shimizu T. T., Barger A. J., Cowie L. L., 2014, *ApJ*, **794**, 152
 Mor R., Netzer H., 2012, *MNRAS*, **420**, 526
 Mor R., Trakhtenbrot B., 2011, *ApJ*, **737**, L36
 Mullaney J. R., Alexander D. M., Goulding A. D., Hickox R. C., 2011, *MNRAS*, **414**, 1082
 Mullaney J. R., et al., 2012, *ApJ*, **753**, L30
 Mullaney J. R., et al., 2015, *MNRAS*, **453**, L83
 Netzer H., 2009, *MNRAS*, **399**, 1907
 Netzer H., 2013, *The Physics and Evolution of Active Galactic Nuclei*
 Netzer H., 2015, *ARA&A*, **53**, 365
 Netzer H., et al., 2007, *ApJ*, **666**, 806
 Netzer H., Mor R., Trakhtenbrot B., Shemmer O., Lira P., 2014, *ApJ*, **791**, 34
 Netzer H., Lani C., Nordon R., Trakhtenbrot B., Lira P., Shemmer O., 2016, *ApJ*, **819**, 123
 Petric A. O., Ho L. C., Flagey N. J. M., Scoville N. Z., 2015, *ApJS*, **219**, 22
 Pilbratt G. L., et al., 2010, *A&A*, **518**, L1
 Polletta M. d. C., et al., 2006, *ApJ*, **642**, 673
 Polletta M., et al., 2007, *ApJ*, **663**, 81
 Reines A. E., Volonteri M., 2015, *ApJ*, **813**, 82
 Rodighiero G., et al., 2011, *ApJ*, **739**, L40
 Rosario D. J., et al., 2012, *A&A*, **545**, A45
 Rosario D. J., et al., 2013, *ApJ*, **771**, 63
 Roussel H., Sauvage M., Vigroux L., Bosma A., 2001, *A&A*, **372**, 427
 Rovilos E., et al., 2012, *A&A*, **546**, A58
 Santini P., et al., 2012, *A&A*, **540**, A109
 Schmidt M., Green R. F., 1983, *ApJ*, **269**, 352
 Shankar F., et al., 2016, *MNRAS*, **460**, 3119
 Shi Y., et al., 2007, *ApJ*, **669**, 841
 Shi Y., Rieke G. H., Ogle P. M., Su K. Y. L., Balog Z., 2014, *ApJS*, **214**, 23
 Shimizu T. T., Mushotzky R. F., Meléndez M., Koss M. J., Barger A. J., Cowie L. L., 2016, preprint, ([arXiv:1612.03941](https://arxiv.org/abs/1612.03941))
 Skrutskie M. F., et al., 2006, *AJ*, **131**, 1163
 Smith J. D. T., et al., 2007, *ApJ*, **656**, 770
 Stalevski M., Ricci C., Ueda Y., Lira P., Fritz J., Baes M., 2016, *MNRAS*, **458**, 2288
 Stanley F., Harrison C. M., Alexander D. M., Swinbank A. M., Aird J. A., Del Moro A., Hickox R. C., Mullaney J. R., 2015, *MNRAS*, **453**, 591
 Sturm E., Lutz D., Tran D., Feuchtgruber H., Genzel R., Kunze D., Moorwood A. F. M., Thornley M. D., 2000, *A&A*, **358**, 481
 Symeonidis M., Giblin B. M., Page M. J., Pearson C., Bendo G., Seymour N., Oliver S. J., 2016, *MNRAS*, **459**, 257
 Trakhtenbrot B., Netzer H., 2010, *MNRAS*, **406**, L35
 Tsai C.-W., et al., 2015, *ApJ*, **805**, 90

- Ueda Y., Akiyama M., Ohta K., Miyaji T., 2003, *ApJ*, **598**, 886
 Veilleux S., et al., 2009, *ApJ*, **701**, 587
 Whitaker K. E., van Dokkum P. G., Brammer G., Franx M., 2012, *ApJ*, **754**, L29
 Willner S. P., Soifer B. T., Russell R. W., Joyce R. R., Gillett F. C., 1977, *ApJ*, **217**, L121
 Wright E. L., et al., 2010, *AJ*, **140**, 1868
 Wu H., Cao C., Hao C.-N., Liu F.-S., Wang J.-L., Xia X.-Y., Deng Z.-G., Young C. K.-S., 2005, *ApJ*, **632**, L79
 Xu L., Rieke G. H., Egami E., Pereira M. J., Haines C. P., Smith G. P., 2015, *ApJS*, **219**, 18
 Zhang Z., Shi Y., Rieke G. H., Xia X., Wang Y., Sun B., Wan L., 2016, *ApJ*, **819**, L27
 van der Wel A., et al., 2014, *ApJ*, **788**, 28

APPENDIX A: COMPARISON TO SYMEONIDIS ET AL. (2016)

Here we focus on the lower redshift ($z < 0.18$) sub-sample of PG QSOs considered in S16. A detailed description of the selection criteria for this sub-sample is given in S16. Briefly, as well as the redshift cut, they required radio-quietness and $L_{2\text{KeV}-1\mu\text{m}} > 10 \times L_{8-1000\mu\text{m}}$. This part of our analysis is based on 43 sources, identified from the names provided in Figure 3 of S16. Our sample size differs from that of S16 (47 QSOs) because we excluded 1 source due to having upper limits in all 3 *Herschel*/PACS bands, and 3 sources for having atypically-looking torus emission in the near- and mid-IR.

When considering the lower redshift PG QSOs sub-sample, we identify a colder median intrinsic AGN SED than the EM12 median, yet warmer than that presented in S16. This is shown in Figure A1, and is in agreement with the results presented in §3.3 for the overall population. If, however, we follow the same procedure as S16, i.e. finding the mean observed AGN SED without normalization and subtracting from it the mean SF template, we recover an intrinsic AGN SED that is consistent with that found in S16. We here stress the importance of normalising the considered SEDs before calculating their average, when seeking to study SED shapes.

To quantify the effect that the lack of normalisation has on the calculation of the mean SED, we calculated the ratio between the average sample luminosity at $70\mu\text{m}$ and the average sample luminosity at $12\mu\text{m}$ ($\langle L_{70\mu\text{m}} \rangle / \langle L_{12\mu\text{m}} \rangle$). We find that this quantity increases by ~ 35 per cent when it is calculated on the un-normalised SF-subtracted SEDs, compared to the normalised SF-subtracted SEDs. Furthermore we find this ratio to be extremely sensitive to the most luminous sources ($L_{70\mu\text{m}} > 3 \times 10^{44}$ erg/s – 4 PG quasars) when not normalizing the SF-subtracted SEDs. Upon discarding the 4 most luminous sources, $\langle L_{70\mu\text{m}} \rangle / \langle L_{12\mu\text{m}} \rangle$ decreases by ~ 46 per cent in the un-normalised case, and by ~ 16 per cent in the normalised case. This indicates that the mean intrinsic AGN SED proposed by S16 represents mostly the sources with the largest $L_{70\mu\text{m}}$ in the sub-sample of $z < 0.18$ PG quasars, rather than the entire population.

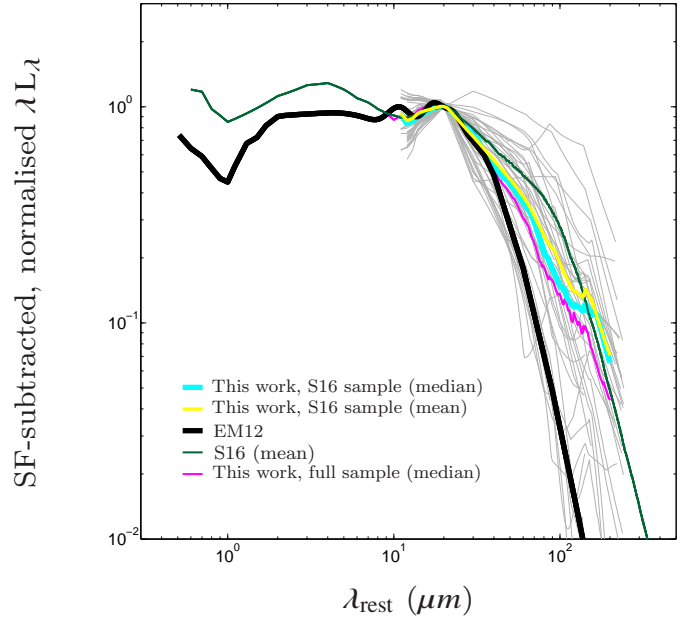


Figure A1. Normalised SF-subtracted SEDs for the $z < 0.18$ sub-sample of PG QSOs considered in S16. This resulting median SED (cyan) is consistent with that derived from the full population (magenta), and differs from that found by S16 (green). We attribute this difference mostly to the lack of normalisation of the SF-subtracted SEDs prior to the calculation of the mean in S16, and the presence of a few sources with extremely high $L_{70\mu\text{m}}/L_{12\mu\text{m}}$. The mean of the S16 sample calculated after normalisation (yellow line) is closer to our median than to the mean S16 SED.

APPENDIX B: THE PAH-BASED INTRINSIC AGN SED USING AN ALTERNATIVE SET OF SF TEMPLATES

Here we check whether the choice of SF library in the derivation of the PAH-based intrinsic AGN SED impacts on the result. In this exercise we follow the same method as highlighted in §3.3, but we consider the DH02 library of SF templates. The result is shown in Figure B1 and is consistent with that presented in §3.3.

APPENDIX C: COMPARISON BETWEEN EM12 AND ME15

Figure C1 shows in black the median EM12 intrinsic AGN SED (with 25th and 75th percentiles in grey), and in red the intrinsic AGN SED from Xu et al. (2015), as shown in Lyu et al. (2017). The two templates, which are both normalised at $5\mu\text{m}$ agree long-ward of $\sim 2\mu\text{m}$, with small differences.

APPENDIX D: INTRINSIC AGN SEDS

Below we provide the data for the intrinsic AGN SEDs considered in this work. We note that for the PAH-based SEDs we do not provide data short-ward of $20\mu\text{m}$ as below this wavelength we assume the EM12 SED (e.g. in §4.4).

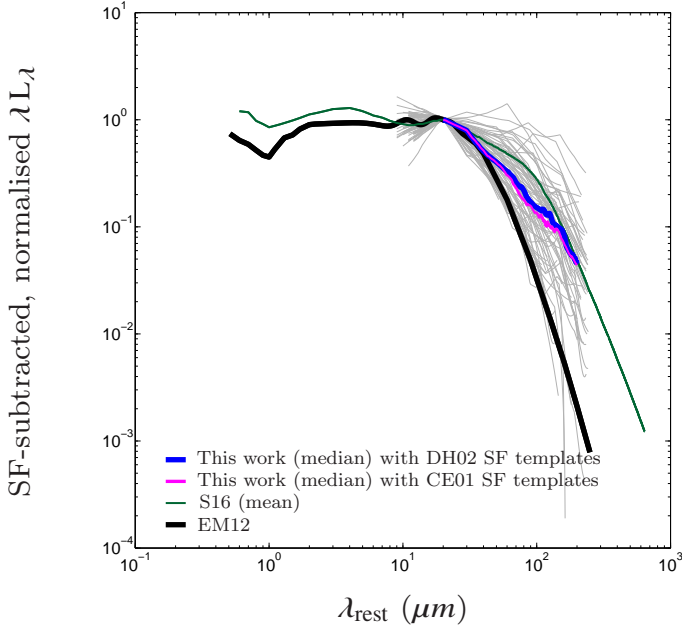


Figure B1. Same as Figure 5, but here we have subtracted the DH02 SF templates to obtain SF-subtracted intrinsic AGN SEDs of our PGs. Regardless of the SF library considered we obtain consistent median intrinsic AGN SEDs

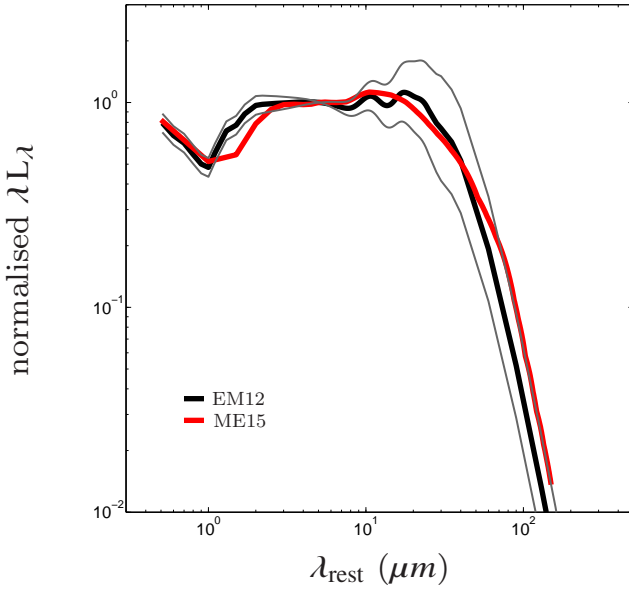


Figure C1. Comparison between the EM12 intrinsic AGN SED (black, with 25th and 75th percentiles in grey) and that from Xu et al. (2015, red), which we refer to as ME15. For wavelengths longer than $\lambda = 2\mu\text{m}$ the two SEDs appear in agreement within the uncertainties.

Furthermore, the EM12 template is identical to that given in Mor & Netzer (2012) for wavelength $\lambda > 2.2\mu\text{m}$, while at shorter wavelengths the interpolation considered here is slightly different from that in Mor & Netzer (2012).

This paper has been typeset from a $\text{\TeX}/\text{\LaTeX}$ file prepared by the author.

Rest wavelength λ_{rest} (μm)	Extended EM12 median intrinsic AGN SED J_{L_1} (arbitrary units)	Extended EM12 25 th percentile J_{L_1} (arbitrary units)	Extended EM12 75 th percentile J_{L_1} (arbitrary units)	Median, PAH-based intrinsic AGN SED for full PG sample J_{L_1} (arbitrary units)	25 th percentile for full PG sample (PAH-based) J_{L_1} (arbitrary units)	75 th percentile for full PG sample (PAH-based) J_{L_1} (arbitrary units)	Median, PAH-based intrinsic AGN SED for "top 1 σ " PGs J_{L_1} (arbitrary units)
1.00	0.4487	0.2731	0.7372				
2.00	0.9010	0.5484	1.4802				
3.00	0.9262	0.5841	1.4687				
4.00	0.9370	0.6112	1.4364				
5.00	0.9322	0.6283	1.3832				
6.00	0.9111	0.6338	1.3038				
7.00	0.8821	0.6328	1.2296				
8.00	0.8752	0.6469	1.1841				
9.00	0.9220	0.7015	1.2118				
10.00	0.9838	0.7699	1.2571				
11.00	0.9971	0.8020	1.2396				
12.00	0.9537	0.7878	1.1545				
13.00	0.9080	0.7698	1.0709				
14.00	0.9033	0.7855	1.0388				
15.00	0.9418	0.8395	1.0567				
16.00	0.9998	0.9129	1.0950				
17.00	1.0389	0.9711	1.1114				
18.00	1.0406	0.9953	1.0879				
19.00	1.0226	1.0004	1.0453				
20.00	1.0000	1.0000	1.0000	1.0000	1.0000	1.0000	1.0000
21.00	0.9824	1.0038	0.9615	0.9837	0.9717	1.0049	1.0031
22.00	0.9675	1.0096	0.9272	0.9530	0.9495	0.9779	0.9930
23.00	0.9432	1.0047	0.8854	0.9285	0.9025	0.9627	0.9820
24.00	0.9049	0.9836	0.8325	0.9048	0.8637	0.9391	0.9636
25.00	0.8561	0.9492	0.7722	0.8847	0.8210	0.9199	0.9512
26.00	0.8139	0.9201	0.7200	0.8653	0.7888	0.9060	0.9390
27.00	0.7743	0.8921	0.6720	0.8470	0.7600	0.8906	0.9268
28.00	0.7391	0.8676	0.6296	0.8286	0.7328	0.8746	0.9153
29.00	0.7164	0.8567	0.5991	0.8116	0.7016	0.8600	0.9048
30.00	0.6951	0.8462	0.5710	0.7935	0.6716	0.8463	0.8943
31.00	0.6733	0.8197	0.5531	0.7531	0.6501	0.8225	0.8820
32.00	0.6528	0.7947	0.5362	0.7120	0.6311	0.7989	0.8699
33.00	0.6336	0.7713	0.5204	0.6780	0.6090	0.7753	0.8594
34.00	0.6154	0.7492	0.5055	0.6545	0.5858	0.7579	0.8491
35.00	0.5983	0.7284	0.4915	0.6298	0.5624	0.7358	0.8388
36.00	0.5721	0.6965	0.4700	0.6006	0.5335	0.7161	0.8286
37.00	0.5478	0.6668	0.4499	0.5785	0.5048	0.6997	0.8185
38.00	0.5250	0.6392	0.4313	0.5517	0.4832	0.6899	0.8084
39.00	0.5038	0.6133	0.4138	0.5301	0.4572	0.6805	0.7983
40.00	0.4839	0.5891	0.3975	0.5174	0.4322	0.6696	0.7884
41.00	0.4556	0.5546	0.3742	0.4958	0.4103	0.6580	0.7785
42.00	0.4295	0.5229	0.3528	0.4754	0.3905	0.6467	0.7687
43.00	0.4055	0.4936	0.3331	0.4586	0.3740	0.6352	0.7590
44.00	0.3833	0.4666	0.3149	0.4539	0.3557	0.6226	0.7493
45.00	0.3628	0.4417	0.2980	0.4418	0.3385	0.6103	0.7397
46.00	0.3438	0.4186	0.2824	0.4323	0.3223	0.5984	0.7302
47.00	0.3262	0.3971	0.2679	0.4250	0.3097	0.5868	0.7226
48.00	0.3098	0.3772	0.2545	0.4178	0.3070	0.5804	0.7160
49.00	0.2946	0.3586	0.2420	0.4062	0.2986	0.5760	0.7096
50.00	0.2804	0.3413	0.2303	0.3976	0.2860	0.5678	0.7063
51.00	0.2671	0.3252	0.2194	0.3866	0.2729	0.5591	0.7006
52.00	0.2547	0.3101	0.2092	0.3789	0.2616	0.5496	0.6947
53.00	0.2431	0.2960	0.1997	0.3746	0.2528	0.5498	0.6890
54.00	0.2323	0.2828	0.1908	0.3649	0.2429	0.5422	0.6835
55.00	0.2221	0.2703	0.1824	0.3555	0.2311	0.5348	0.6782
56.00	0.2125	0.2587	0.1745	0.3454	0.2194	0.5224	0.6731
57.00	0.2035	0.2477	0.1672	0.3332	0.2098	0.5094	0.6681
58.00	0.1950	0.2374	0.1602	0.3246	0.2000	0.4967	0.6634
59.00	0.1870	0.2277	0.1536	0.3129	0.1914	0.4843	0.6568
60.00	0.1795	0.2185	0.1474	0.3050	0.1842	0.4744	0.6457
61.00	0.1702	0.2071	0.1398	0.3011	0.1825	0.4696	0.6378
62.00	0.1614	0.1965	0.1326	0.2950	0.1722	0.4684	0.6365
63.00	0.1533	0.1866	0.1259	0.2890	0.1649	0.4645	0.6358
64.00	0.1457	0.1774	0.1197	0.2832	0.1561	0.4596	0.6355
65.00	0.1386	0.1687	0.1138	0.2768	0.1454	0.4514	0.6352
66.00	0.1319	0.1606	0.1083	0.2698	0.1395	0.4410	0.6318
67.00	0.1256	0.1530	0.1032	0.2533	0.1341	0.4365	0.6291
68.00	0.1198	0.1458	0.0984	0.2456	0.1289	0.4243	0.6118
69.00	0.1142	0.1391	0.0938	0.2422	0.1245	0.4133	0.6014
70.00	0.1091	0.1328	0.0896	0.2327	0.1200	0.4014	0.5913
71.00	0.1042	0.1268	0.0856	0.2284	0.1159	0.3917	0.5816
72.00	0.0996	0.1212	0.0818	0.2212	0.1102	0.3811	0.5699
73.00	0.0952	0.1159	0.0782	0.2122	0.1043	0.3710	0.5562
74.00	0.0911	0.1109	0.0749	0.2034	0.0995	0.3607	0.5427
75.00	0.0873	0.1062	0.0717	0.1962	0.0941	0.3499	0.5296
76.00	0.0836	0.1018	0.0687	0.1913	0.0919	0.3394	0.5168
77.00	0.0801	0.0976	0.0659	0.1902	0.0899	0.3297	0.5045
78.00	0.0769	0.0936	0.0631	0.1824	0.0862	0.3222	0.4921
79.00	0.0738	0.0898	0.0606	0.1845	0.0838	0.3150	0.4801
80.00	0.0708	0.0862	0.0582	0.1814	0.0809	0.3051	0.4751

Table D1: Data for the intrinsic AGN SEDs considered in our work.

Rest wavelength λ_{rest} (μm)	Extended EM12 median intrinsic AGN SED λ_{L_4} (arbitrary units)	Extended EM12 25^{th} percentile λ_{L_4} (arbitrary units)	Extended EM12 75^{th} percentile λ_{L_4} (arbitrary units)	Median, PAH-based intrinsic AGN SED for full PG sample λ_{L_4} (arbitrary units)	25^{th} percentile for full PG sample (PAH-based) λ_{L_4} (arbitrary units)	75^{th} percentile for full PG sample (PAH-based) λ_{L_4} (arbitrary units)	Median, PAH-based intrinsic AGN SED for "top 1 σ " PGs λ_{L_4} (arbitrary units)
81.00	0.0680	0.0828	0.0559	0.1776	0.0789	0.2962	0.4714
82.00	0.0654	0.0796	0.0537	0.1726	0.0771	0.2880	0.4677
83.00	0.0629	0.0765	0.0517	0.1677	0.0746	0.2802	0.4642
84.00	0.0605	0.0736	0.0497	0.1634	0.0715	0.2744	0.4609
85.00	0.0582	0.0709	0.0478	0.1592	0.0694	0.2688	0.4576
86.00	0.0561	0.0682	0.0461	0.1641	0.0661	0.2700	0.4545
87.00	0.0540	0.0657	0.0444	0.1610	0.0630	0.2643	0.4515
88.00	0.0520	0.0634	0.0428	0.1594	0.0632	0.2648	0.4486
89.00	0.0502	0.0611	0.0412	0.1591	0.0649	0.2621	0.4457
90.00	0.0484	0.0589	0.0398	0.1566	0.0678	0.2575	0.4431
91.00	0.0464	0.0565	0.0382	0.1553	0.0668	0.2506	0.4409
92.00	0.0446	0.0543	0.0366	0.1512	0.0684	0.2427	0.4380
93.00	0.0428	0.0521	0.0352	0.1472	0.0713	0.2371	0.4301
94.00	0.0412	0.0501	0.0338	0.1434	0.0743	0.2338	0.4210
95.00	0.0396	0.0482	0.0325	0.1406	0.0719	0.2300	0.4113
96.00	0.0381	0.0463	0.0313	0.1378	0.0687	0.2257	0.4016
97.00	0.0366	0.0446	0.0301	0.1351	0.0656	0.2215	0.3925
98.00	0.0353	0.0429	0.0290	0.1357	0.0646	0.2171	0.3837
99.00	0.0339	0.0413	0.0279	0.1365	0.0637	0.2125	0.3753
100.00	0.0327	0.0398	0.0269	0.1355	0.0624	0.2081	0.3673
101.00	0.0315	0.0384	0.0259	0.1321	0.0605	0.2041	0.3596
102.00	0.0304	0.0370	0.0250	0.1287	0.0588	0.2003	0.3523
103.00	0.0293	0.0357	0.0241	0.1254	0.0572	0.1966	0.3453
104.00	0.0283	0.0344	0.0232	0.1223	0.0556	0.1943	0.3386
105.00	0.0273	0.0332	0.0224	0.1218	0.0542	0.1922	0.3321
106.00	0.0263	0.0320	0.0216	0.1258	0.0528	0.1901	0.3259
107.00	0.0254	0.0309	0.0209	0.1298	0.0514	0.1887	0.3164
108.00	0.0246	0.0299	0.0202	0.1292	0.0507	0.1873	0.3082
109.00	0.0237	0.0289	0.0195	0.1251	0.0501	0.1843	0.3003
110.00	0.0229	0.0279	0.0188	0.1211	0.0495	0.1821	0.2926
111.00	0.0222	0.0270	0.0182	0.1175	0.0491	0.1805	0.2852
112.00	0.0214	0.0261	0.0176	0.1141	0.0486	0.1779	0.2780
113.00	0.0208	0.0253	0.0170	0.1151	0.0482	0.1755	0.2710
114.00	0.0201	0.0244	0.0165	0.1139	0.0478	0.1739	0.2643
115.00	0.0194	0.0237	0.0160	0.1101	0.0474	0.1723	0.2578
116.00	0.0188	0.0229	0.0155	0.1065	0.0474	0.1707	0.2515
117.00	0.0182	0.0222	0.0150	0.1039	0.0471	0.1693	0.2460
118.00	0.0177	0.0215	0.0145	0.1037	0.0477	0.1678	0.2407
119.00	0.0171	0.0208	0.0141	0.1008	0.0482	0.1664	0.2356
120.00	0.0166	0.0202	0.0136	0.1029	0.0494	0.1642	0.2306
121.00	0.0161	0.0196	0.0132	0.1114	0.0527	0.1635	0.2258
122.00	0.0156	0.0190	0.0128	0.1093	0.0514	0.1614	0.2212
123.00	0.0151	0.0184	0.0124	0.1073	0.0540	0.1602	0.2167
124.00	0.0147	0.0179	0.0121	0.1053	0.0533	0.1602	0.2123
125.00	0.0143	0.0174	0.0117	0.1033	0.0526	0.1602	0.2080
126.00	0.0138	0.0168	0.0114	0.1014	0.0520	0.1592	0.2039
127.00	0.0134	0.0164	0.0110	0.0996	0.0514	0.1583	0.1999
128.00	0.0131	0.0159	0.0107	0.0978	0.0508	0.1573	0.1970
129.00	0.0127	0.0154	0.0104	0.0994	0.0503	0.1573	0.1949
130.00	0.0123	0.0150	0.0101	0.1012	0.0499	0.1575	0.1929
131.00	0.0120	0.0146	0.0098	0.1001	0.0498	0.1578	0.1910
132.00	0.0116	0.0141	0.0095	0.0973	0.0505	0.1569	0.1893
133.00	0.0113	0.0137	0.0093	0.0947	0.0500	0.1537	0.1877
134.00	0.0109	0.0133	0.0090	0.0921	0.0495	0.1536	0.1861
135.00	0.0106	0.0129	0.0087	0.0897	0.0493	0.1536	0.1846
136.00	0.0103	0.0126	0.0085	0.0893	0.0491	0.1531	0.1831
137.00	0.0100	0.0122	0.0082	0.0899	0.0475	0.1520	0.1817
138.00	0.0097	0.0119	0.0080	0.0865	0.0477	0.1519	0.1797
139.00	0.0095	0.0115	0.0078	0.0849	0.0472	0.1518	0.1771
140.00	0.0092	0.0112	0.0076	0.0832	0.0468	0.1523	0.1746
141.00	0.0090	0.0109	0.0074	0.0867	0.0508	0.1547	0.1722
142.00	0.0087	0.0106	0.0072	0.0837	0.0486	0.1557	0.1729
143.00	0.0085	0.0103	0.0070	0.0952	0.0466	0.1567	0.1688
144.00	0.0082	0.0100	0.0068	0.0833	0.0456	0.1547	0.1663
145.00	0.0080	0.0098	0.0066	0.0915	0.0446	0.1529	0.1661
146.00	0.0078	0.0095	0.0064	0.0908	0.0436	0.1530	0.1659
147.00	0.0076	0.0093	0.0062	0.0902	0.0427	0.1520	0.1657
148.00	0.0074	0.0090	0.0061	0.0873	0.0414	0.1446	0.1656
149.00	0.0072	0.0088	0.0059	0.0856	0.0408	0.1422	0.1635
150.00	0.0070	0.0086	0.0058	0.0839	0.0399	0.1399	0.1591
151.00	0.0068	0.0083	0.0056	0.0815	0.0377	0.1384	0.1826
152.00	0.0067	0.0081	0.0055	0.0800	0.0372	0.1362	0.1818
153.00	0.0065	0.0079	0.0053	0.0773	0.0346	0.1348	0.1975
154.00	0.0063	0.0077	0.0052	0.0761	0.0341	0.1331	0.1936
155.00	0.0062	0.0075	0.0051	0.0760	0.0384	0.1322	0.1888
156.00	0.0060	0.0073	0.0050	0.0752	0.0390	0.1307	0.1861
157.00	0.0059	0.0072	0.0048	0.0739	0.0387	0.1285	0.1825
158.00	0.0057	0.0070	0.0047	0.0727	0.0384	0.1264	0.1790
159.00	0.0056	0.0068	0.0046	0.0715	0.0379	0.1243	0.1756
160.00	0.0055	0.0066	0.0045	0.0703	0.0370	0.1222	0.1723

Table D1: Table D1 continued. The full table (with data up to $\lambda = 250 \mu\text{m}$) will be provided in electronic form.